Garau, M, Nieves, MJ and Jones, IS

 Alternating strain regimes for failure propagation in flexural systems

http://researchonline.ljmu.ac.uk/id/eprint/10882/

Article

Alternating strain regimes for failure propagation in flexural systems

M. Garau*, M.J. Nieves*,†and I.S. Jones‡

Abstract

We consider both analytical and numerical studies of a steady-state fracture process inside a discrete mass-beam structure, composed of periodically placed masses connected by Euler-Bernoulli beams. A fault inside the structure is assumed to propagate with a constant speed and this occurs as a result of the action of a remote sinusoidal, mechanical load. The established regime of fracture corresponds to the case of an alternating generalised strain regime. The model is reduced to a Wiener-Hopf equation and its solution is presented. We determine the minimum feeding wave energy required for the steady-state fracture process to occur. In addition, we determine the dynamic features of the structure during the steady-state fracture regime. The transient analysis of this problem is also presented, where the existence of the steady-state fracture regimes revealed by the analytical model are verified and the associated transient features of this process are discussed.

Keywords : Discrete periodic media, mass-beam structures, fracture, Wiener-Hopf technique, numerical simulations.

1 Introduction

The modelling of structured flexural materials is a useful tool in understanding the behaviour of structures commonly found in civil engineering, such as buildings, bridges, rooftops, pipeline systems and many more. The need to understand the response of such structures, as shown in Figure 1, is greater when failure initiates and propagates through the system.

We present a simplified analytical and numerical model to represent the failure of a long bridge or a rooftop. The structure is modelled by Euler-Bernoulli beams connecting periodically placed masses, where the failure is assumed propagate steadily within the structure.

The modelling of failure in structured materials has been widely developed for the analysis of mass-spring systems. These models help in describing several microstructural processes which occur in the fracture of materials [1]. Dynamic Mode III fracture of a square cell lattice composed of massless springs connecting periodically placed masses has been considered in [2]. For discrete mass-spring structures which undergo phase transition processes at a uniform rate, see [3]. Dynamic fracture modes in elastic triangular lattices were treated in [4] for a homogeneous lattice and in [5] for an anisotropic lattice. In these models, the micro-level processes involved in the fracture phenomenon can be identified that include effects such as wave radiation occurring when failure propagates. The introduction of inertial links in the lattice brings new features in terms of these

---

*Keele University, School of Computing and Mathematics, Keele, ST5 5BG, UK

†University of Cagliari, Department of Mechanical, Chemical and Material Engineering, Cagliari, 09123, Italy

‡Mechanical Engineering and Materials Research Centre, Liverpool John Moores University, James Parsons Building, Byrom Street, Liverpool L3 3AF, U.K.

Figure 1: In (a) the demolition of a bridge Guangxi, China. The excavator in this picture was used to initiate some failure at one end of the bridge propagates through the structure. The figure shows the resulting periodic failure process, where the supporting columns fail sequentially causing the collapse of the bridge. An alternative view of this process is presented in (b).

wave radiation processes that can accompany the crack growth, as demonstrated for Mode III fracture inside an inertial square cell lattice in [6].

In addition to the analytical models considered in [2, 3, 4, 6], numerical modelling of Mode I and II crack growth inside strips of triangular lattice has been carried out in [7], where some surprising periodic patterns of fault propagation were observed.

Lattices, composed of fundamental mechanical elements, can easily be designed to produce a variety of media capable of controlling the flow of waves for different applications. In particular, the introduction of structural heterogeneities may influence the admissible regimes where steady crack propagation is possible. The effects of inhomogeneities on Mode III crack propagation in two-dimensional lattices have been analysed in [8].

Structured inhomogeneities in mass-spring lattices have been shown to enhance fracture propagation in [9]. The failure mechanism is caused by a "knife wave" or localised deformation surrounding the crack, capable of sustaining crack propagation within the interface. Numerical simulations of a crack growing through a high-contrast interface were later carried out in [10]. Moreover, these numerical simulations revealed that non-steady failure regimes such as clustering, where a crack may propagate in an unusual way.

Other failure processes propagating in a lattice have been considered in [11], where the extraction of a mass-spring chain due to a point force was considered. The study of a propagating bridge crack in an inhomogeneous lattice has been carried out in [12].

Different fracture criteria, independent of or dependent on time, can produce a variety of fracture patterns within lattice systems and can also affect the existence of admissible steady-state fracture regimes. The impact of time dependent fracture criteria on the failure of one-dimensional mass-spring chains has been investigated in [13].

The important question of admissibility of unstable and stable crack regimes for cracks propagating in discrete periodic media has been discussed in [1, 14, 15]. The existence of admissible steady-state regimes at low velocities that propagate through a mass-spring square cell lattice [15] has recently been re-addressed in [16]. The influence of a moving load on Mode III fracture regimes in a discrete mass-spring structure has been analytically and numerically studied in [17]. Failure regimes in discrete structures with non-local interactions and their effects on the wave radiation processes are presented in [18].

In contrast to the study of dynamic fracture in mass-spring systems, very few articles concentrate on the failure of systems incorporating flexural elements such as beams. The study of bending modes
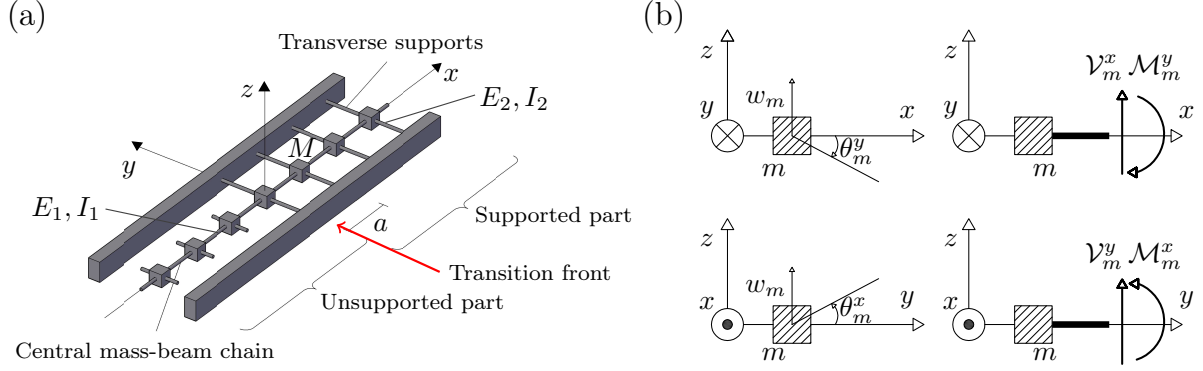
Figure 2: (a) A heterogeneous discrete structure composed of point masses. (b) The convention adopted for positive direction of displacements w_m, rotation θ_m associated with the mth mass. The positive directions for the internal bending moments $\mathcal{M}_m^y$, $(\mathcal{M}_m^x)$ and shear forces $\mathcal{V}_m^x$, $(\mathcal{V}_m^y)$ in the mth beam directed from the mth mass in the positive x-direction (y-direction) are also indicated.

in 2D discrete flexural structures, composed of masses and beams, containing static faults can be found in [19]. One-dimensional mass-beam chains supported by an elastic foundation, have been used to create a simplified model of a collapsing bridge [20]. This model has been further developed in [21] and used to predict the collapse rate of the San-Saba rail road bridge, Texas, in 2013. Transition waves in continuous flexural systems have been shown to exhibit surprising non-steady failure behaviour [22].

Experimentally, one can observe counter-intuitive fracture behaviour in elastic materials such as rubber sheets [23], where analytical descriptions and numerical simulations of this process have been given in [24].

In [25], an analytical model for the failure of a discrete flexural structure contained within an interface, was studied. The fracture was assumed to be caused by a remote sinusoidal load and the dynamic features of the structure, during the fracture process, were studied. Further, in [26] the transient failure process was numerically modelled and the results of [25] were verified.

Here, we consider failure propagation within the mass-beam structure shown in Figure 2. The failure is represented by the sequential removal of links supporting the masses along the central chain, aligned with the horizontal axis. In [25, 26], the failure process was investigated under the assumption the supporting columns of the central chain are removed if the masses achieve a positive critical displacement. These steady-state regimes achieved in this case are referred to here as "*pure steady-state regimes*" and assumed to be driven by a remote mechanical sinusoidal load. In terms of applications, it is realistic to consider the case when the supporting links break if a positive or negative critical displacement is reached. As we show here, along with the *pure steady-state regimes* observed in [25, 26], the imposed fracture criterion yields additional regimes, which can be predicted and verified numerically. These regimes correspond to the case when one can observe a change in the sign of the bending moments and shear forces in the supporting beams over a fixed time interval. These regimes are investigated in detail here and are referred to as "*alternating generalised strain regimes*".

The structure of the present article is as follows. In Section 2, we present an analytical description of the problem concerning failure propagation in the mass-beam structure subjected to a sinusoidal load. This section also includes the reduction of the problem to a functional equation of the Wiener-Hopf type. From this the alternating generalised strain regimes can be identified. The description

3

of the dispersive nature of this particular discrete structure is given in Section 3. The results of Section 3 are then used in Section 4 to solve the Wiener-Hopf equation. We also identify the dynamic properties of the structure during the steady propagation of the alternating generalised strain regime in Section 5. In Section 6, we present numerical simulations which verify the analytical results of Sections 2–5. We give some conclusions and discussion in Section 7. Finally, Appendices A and B contain details of some derivations.

2 Model of failure within a discrete periodic flexural structure

2.1 Description of the problem

We consider a structure composed of a mass-beam chain, as shown in Figure 2(a). This structure is formed from periodically placed point masses, connected longitudinally (along x-axis) by massless Euler-Bernoulli beams all with Young's modulus E_1 and second moment of area J_1. Each junction node has mass M and corresponds to an index $m \in \mathbb{Z}$. This chain is assumed to be partially supported by transverse Euler-Bernoulli beams (parallel to the y-axis), having Young's modulus E_2 and second moment of area J_2. These beams connect the masses to an interface where the beams are clamped. All beams have length a.

Inside the structure, failure is assumed to propagate with a uniform speed V as result of the breakage of the transverse connections to the interfaces within the structure. This breakage occurs when the *absolute value* of the displacement w_p of the pth mass (where $m = p$ corresponds to the position of the transition front in the structure, see Figure 2(a)) reaches a critical value w_c. Thus we assume for bonds to remain intact

$$|w_j(t)| < w_c, \quad j \geq p, \quad p \in \mathbb{Z}. \tag{1}$$

and when the condition $w_p = \pm w_c$ is fulfilled, the transverse links at the pth-mass break and the moving interface advances a distance a in the structure to the $(p+1)^{\text{th}}$ node.

The condition (1) enable us to exclude the case of non-steady propagation of the interface inside the structure. Under these assumptions, we consider the case when the *generalised strains* (moments and shear forces) inside the transverse links alternate in sign during the failure process.

2.2 Governing equations

At a given time t, the position of the interface in the structure is given by $m = Vt/a$. Here, the inequality $ma \geq Vt$ corresponds to masses located in the supported part of the structure and $ma < Vt$ are those in the unsupported region of the structure (see Figure 2).

The equations for the balance of linear and angular momentum for the mth mass, $m \in \mathbb{Z}$, are

$$M \frac{\mathrm{d}^2 w_m(t)}{\mathrm{d}t^2} = \mathcal{V}_m^x(0,t) - \mathcal{V}_{m-1}^x(a,t) + H(x - Vt)(\mathcal{V}_m^{y,+}(0,t) - \mathcal{V}_m^{y,-}(a,t)) + Q_m(t), \tag{2}$$

$$\mathcal{M}_m^y(0,t) = \mathcal{M}_m^y(a,t), \tag{3}$$

where H is the Heaviside function

$$H(x) = \begin{cases} 1, & \text{if } x \geq 0, \\ 0, & \text{otherwise}. \end{cases}$$

In (2) and (3), $\mathcal{M}_m^y(\tilde{x},t)$ and $\mathcal{V}_m^x(\tilde{x},t)$, denote the y-component of the moment vector and shear forces in the mth horizontal beam, respectively, at time t, where $0 < \tilde{x} < a$, (see Figure 2(b)). They

can be written in terms of the generalised coordinates describing the motion of the mth mass as

$$\mathcal{M}_m^y(\tilde{x},t) = -\frac{2E_1J_1}{a^3}[a^2\theta_m^y(t) + a(a-3\tilde{x})(\theta_m^y(t) + \theta_{m+1}^y(t)) - 3(2\tilde{x}-a)(w_{m+1}(t) - w_m(t))] \quad (4)$$

$$\mathcal{V}_m^x(\tilde{x},t) = \frac{6E_1J_1}{a^3}[a(\theta_m^y(t) + \theta_{m+1}^y(t)) - 2(w_m(t) - w_{m+1}(t))] \,, \quad (5)$$

where w_m is the displacement and θ_m^y is the rotation about the y-axis of the mth mass (see Appendix A for the derivation of (4) and (5)). In a similar way, the shear forces $\mathcal{V}_j^{y,+}(y,t)$ and $\mathcal{V}_j^{y,-}(y,t)$ correspond to those in the transverse beam above and below, respectively, the jth mass where $j \geq Vt/a$. As discussed in Appendix A, they take the form

$$\mathcal{V}_m^{y,\pm}(y_\pm,t) = \mp\frac{12E_2J_2}{a^3}w_m(t) \,. \quad (6)$$

In (2), the term $Q_m(t)$ is the applied load at a node m. The angular momentum balance about the x-axis for a mass in the supported region, shows the masses do not rotate about about the x-axis. This is proved in Appendix A.

Equations (2) and (3) then become

$$6\left\{2[2w_m(t) - w_{m-1}(t) - w_{m+1}(t)] - a[\theta_{m+1}^y(t) - \theta_{m-1}^y(t)]\right\}$$
$$+ 24rw_m(t)H(m-Vt/a) + \frac{Ma^3}{E_1I_1}\frac{\mathrm{d}^2w_m(t)}{\mathrm{d}t^2} = \frac{a^3}{E_1J_1}Q_m(t)\,, \quad (7)$$

and

$$3[w_{m+1}(t) - w_{m-1}(t)] + a[\theta_{m+1}^y(t) + \theta_{m-1}^y(t) + 4\theta_m^y(t)] = 0\,, \quad (8)$$

where the contrast parameter $r = E_2J_2/E_1J_1$.

2.3 Derivation of the Wiener-Hopf equation

Since we consider the case of alternating generalised strains, we look for the displacements and the rotations as functions of the moving coordinate $\eta = m - Vt/a$ as follows

$$w_m(t) = (-1)^m w(\eta), \quad \theta^y(t) = (-1)^m\theta^y(\eta) \,. \quad (9)$$

In addition, we assume the load takes the form $Q_m(t) = (-1)^m Q(\eta)$.

We introduce the Fourier transforms with respect to the variable η for the quantities w^{F}, $\theta^{y\mathrm{F}}$ as

$$\{w^{\mathrm{F}}, \theta^{y\mathrm{F}}\} = \int_{-\infty}^{\infty}\{w(\eta), \theta^y(\eta)\}e^{ik\eta}d\eta \,,$$

where k is the dimensionless wavenumber. The following "half" transforms are also used:

$$w_\pm(k) = \int_{-\infty}^{\infty} w(\eta)e^{ik\eta}H(\pm\eta)d\eta \,, \quad \pm\mathrm{Im}\,k > 0 \,, \qquad w^{\mathrm{F}} = w_+ + w_- \,.$$

Here w_+ (w_-) corresponds to a function analytic in the upper (lower) half of the complex plane defined by k.

In (7), (8), we make the change of variable $\eta = m - Vt/a$ and introduce the normalisations

$$V = \tilde{v}\sqrt{E_1J_1/Ma}, \quad w(\eta) = a\tilde{w}(\eta), \quad Q(\eta) = \frac{E_1J_1}{a^2}\tilde{Q}(\eta),$$

where the symbol "tilde" will be omitted for ease of notation.

Then after insertion of (9) into (7) and (8) we obtain

$$6\left\{2[2w(\eta) + w(\eta - 1) + w(\eta + 1)] + [\theta^y(\eta + 1) - \theta^y(\eta - 1)]\right\}$$

$$+ 24rw(\eta)H(\eta) + v^2\frac{\mathrm{d}^2 w(\eta)}{\mathrm{d}\eta^2} = Q(\eta), \quad (10)$$

and

$$-3[w(\eta + 1) - w(\eta - 1)] + [4\theta^y(\eta) - \theta^y(\eta + 1) - \theta^y(\eta - 1)] = 0. \quad (11)$$

The Fourier transform of (11) with respect to the moving coordinate η leads to

$$\theta^{y\mathrm{F}} = -\frac{3\mathrm{i}\sin(k)}{2 - \cos(k)}w^{\mathrm{F}} \quad (12)$$

and together with the Fourier transform of (10) we then obtain

$$h_1(k, 0 + \mathrm{i}kv)w_+ + h_2(k, 0 + \mathrm{i}kv)w_- = Q^{\mathrm{F}}. \quad (13)$$

where Q^{F} is the Fourier transform of the load Q and

$$h_j(k, Y) = \Omega_j^2(k + \pi) + Y^2, \quad j = 1, 2, \quad (14)$$

$$\Omega_1(k) = \sqrt{\frac{48\sin^4(k/2)}{2 + \cos(k)} + 24r}, \qquad \Omega_2(k) = \sqrt{\frac{48\sin^4(k/2)}{2 + \cos(k)}}. \quad (15)$$

Here the presence of the term $(0 + \mathrm{i}kv)$ in (13) appears as a result of the causality principle discussed in [15], and represents the passing from the transient regime to the steady-state regime in the Laplace transform. Note that the expresssions (15) correspond to dispersion relations for the problem in [25, 26], where the fracture was considered for the pure steady-state failure regimes.

3 Dispersion relations

The dispersive properties of the structure can be determined from the zeros of h_j, $j = 1, 2$, in (13). In replacing Y by $\mathrm{i}\omega$ in (14) and rearranging for ω we obtain the dispersion relations

$$\omega_1(k) = \Omega_1(k + \pi) = \sqrt{\frac{48\cos^4(k/2)}{2 - \cos(k)} + 24r}, \quad (16)$$

for the waves ahead of the transition front and

$$\omega_2(k) = \Omega_2(k + \pi) = \sqrt{\frac{48\cos^4(k/2)}{2 - \cos(k)}}, \quad (17)$$
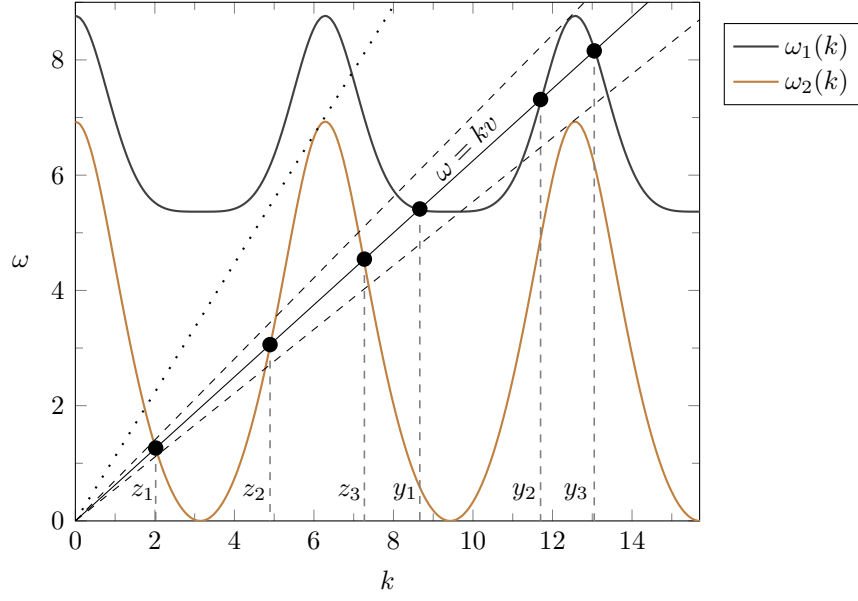
for waves behind the transition front.

Figure 3: Dispersion diagrams for equations (16) and (17) are shown as functions of the wavenumber k for $r = 0.625$. The ray $\omega = kv$ intersects the dispersion curves at points, shown as dots, with the k-coordinates y_1, y_2, y_3 and z_1, z_2, z_3 that are solutions of h_1 and h_2, respectively. The dotted inclined line has the gradient $v_1 = 1.117$ and represents the upper bound of the alternating generalised strain failure regime. The dashed inclined lines represent the bounds for the speeds of possible transmission regimes, where waves propagating ahead of the transition front can occur. The number of such regimes can increase with decrease of the failure speed. Outside these intervals, failure regimes where evanescent waves propagate ahead of the failure are encountered.

Existence of waves in the structure

Waves inside the structure are assumed to propagate as a result of either the external action from a remote load or through dissipation from the transition front. These waves can be identified from the dispersion relations (14). In Figure 3, we give a representative example showing the dispersion curves ω_1 and ω_2 as functions of the wave number k, based on (16)–(17), along with the line $\omega = kv$.

Characterisation of the waves. Intersections of the line defined by $\omega = kv$ with the curve based on the relation ω_1 in (16) represent waves propagating ahead of the transition front ($\eta \geq 0$). Those intersection points of this line with ω_2, given by (17), correspond to waves behind the transition front ($\eta < 0$).

By computing the group velocity of the wave defined by $v_g = d\omega/dk$ at each intersection point, it is possible to determine the direction of propagation of the wave. Any intersection point of the curve given by ω_1 with the line $\omega = kv$ where $v_g < v$ or $v_g > v$, indicates a wave propagating in the supported region towards or away from the transition front, respectively. In a similar way, any intersection of the curve provided by ω_2 with the ray $\omega = kv$ where $v_g > v$ or $v_g < v$ indicates a wave propagating behind the transition point towards or away from the transition front.

Roots of the functions h_j, $1 \leq j \leq 2$. Here we describe, in general, possible roots of the functions h_j, $1 \leq j \leq 2$, which will help to determine the nature of the waves inside the structure. These roots are associated with the intersections of the ray $\omega = kv$ and the curves determined by the functions ω_j, $1 \leq j \leq 2$.

In the following, we consider the speed range $0 < v \leq v_1 = 1.117$. Here the upper bound determines the maximum speed for which the failure process can occur under the alternating generalised strain regime. This upper bound is the slope of the solid inclined line in Figure 3. For the failure process to occur, it is required that there exists one intersection point of the line $\omega = kv$ with the curve ω_2 where $v_g > v$. Such a point defines a wave that can propagate behind and deliver energy to the transition front.

Zeros of h_1. The function $h_1(k, 0 + ikv)$ has one, three or more pairs of zeros at the points $k = \pm y_1 + i0, \pm y_2 - i0, \ldots, \pm y_{2b+1} + i0$, with $b \in \mathbb{Z}$, $b \geq 0$. Here b depends on the speed v and the small imaginary part of the wavenumbers appears as a result of the causality principle [15]. For those points

1. $k = \pm y_1 + i0, \ldots, \pm y_{2b+1} + i0$, the group velocity $v_g < v$ and

2. $k = \pm y_2 - i0, \ldots, \pm y_{2b} - i0$, the group velocity $v_g > v$.

These wave numbers are associated with feeding and reflected waves that appear behind the transition front during the steady failure regime.

Zeros of h_2. The function $h_2(k, 0 + ikv)$ can have three, five or more pairs of simple zeros at $k = \pm z_1 + i0, \pm z_2 - i0, z_3 + i0, \ldots, \pm z_{2l+1} + i0$, $l \in \mathbb{Z}$, $l \geq 1$. Again l is a parameter which depends on the speed v. For

1. $k = \pm z_1 + i0, \pm z_3 + i0, \ldots, \pm z_{2l+1} + i0$, then $v_g < v$,

2. $k = \pm z_2 - i0, \pm z_4 - i0, \ldots, \pm z_{2l} - i0$, then $v_g > v$.

Here, the points with $v_g < v$ correspond to waves produced by a load situated far ahead of the transition front. The points with $v < v_g$ are associated with transmitted waves that propagate ahead of the transition front in the steady-state failure process. These waves can appear for particular failure speeds and an example of an interval of such speeds is shown in Figure 3.

4 The Wiener-Hopf equation and its solution

Here, we develop the solution of (13) for the alternating generalised strain regime. We rewrite this equation in the form

$$w_+ + \frac{\Psi_+(k)}{\Psi_-(k)} L(k) w_- = \frac{Q^{\mathrm{F}}}{h_1(k, 0 + \mathrm{i}kv)} \;, \tag{18}$$

with

$$\Psi_+(k) = \frac{\displaystyle\prod_{i=1}^{l} (0 - \mathrm{i}(k - z_{2i}))(0 - \mathrm{i}(k + z_{2i}))}{(1 - \mathrm{i}k)^{2(l-b)} \displaystyle\prod_{j=1}^{b} (0 - \mathrm{i}(k - y_{2j}))(0 - \mathrm{i}(k + y_{2j}))} \;, \tag{19}$$

$$\Psi_-(k) = \frac{(1 + \mathrm{i}k)^{2(l-b)} \displaystyle\prod_{j=0}^{b} (0 + \mathrm{i}(k - y_{2j+1}))(0 + \mathrm{i}(k + y_{2j+1}))}{\displaystyle\prod_{i=0}^{l} (0 + \mathrm{i}(k - z_{2i+1}))(0 + \mathrm{i}(k + z_{2i+1}))} \;, \tag{20}$$

where $\prod_{j=1}^{0} = 1$ and

$$L(k) = \frac{\Psi_-(k)}{\Psi_+(k)} \frac{h_2(k, 0 + \mathrm{i}kv)}{h_1(k, 0 + \mathrm{i}kv)} \;. \tag{21}$$

Here, $L(k) > 0$ for $k \in \mathbb{R}$ and satisfies the conditions required for its factorisation. That is, for $k \in \mathbb{R}$

$$\mathrm{Re}(L(k)) = \mathrm{Re}(L(-k)) \quad \text{and} \quad \mathrm{Im}(L(k)) = \mathrm{Im}(L(-k)) \;. \tag{22}$$

In addition, $L(k) \to 1$ as $k \to \pm\infty$ and the index of the function $L(k)$ is zero. Then, $L(k)$ can be written using the Cauchy-type factorisation in the form:

$$L(k) = L_+(k) L_-(k) \;, \quad L_\pm(k) = \exp\left(\pm \frac{1}{2\pi\mathrm{i}} \int_{-\infty}^{\infty} \frac{\ln L(\xi)}{\xi - k} \, d\xi \right) \;, \quad \pm\mathrm{Im}(k) > 0 \;.$$

In this representation, the function L_+ (L_-) is analytic in the upper (lower) half of the complex plane defined by k. Then, (18) can be written in the form of the Wiener-Hopf equation

$$\frac{1}{L_+(k)\Psi_+(k)} w_+ + \frac{1}{\Psi_-(k)} L_-(k) w_- = \frac{Q^{\mathrm{F}}}{L_+(k)\Psi_+(k)h_1(k, 0 + \mathrm{i}kv)} \;. \tag{23}$$

4.1 The solution of the Wiener-Hopf equation

As in [15], non-trivial solutions of (23) correspond to singular points on the right-hand side. Such singular points occur when

$$L_+(k)\Psi_+(k)h_1(k, 0 + \mathrm{i}kv) = 0 \;.$$

As $L(k)$ has no real zeros, referring to Section 3 and (19), we note the above left-hand side is only zero when $k = \pm y_{2j+1} - \mathrm{i}0$, $0 \le j \le b$, and $k = \pm z_{2j} - \mathrm{i}0$, $1 \le j \le l$. The points $k = \pm y_{2j+1} - \mathrm{i}0$,

$0 \leq j \leq b$, correspond to the action of a remote force from the left of the transition front as they are associated with the inequality $v_g > v$. On the other hand, the points $k = \pm z_{2j} - \mathrm{i}0$, $1 \leq j \leq l$, represent the loading from the right of the transition front (with $v > v_g$).

Here, we assume that the loading of the structure takes the form of an oscillatory mechanical load. This load is situated remotely on the left of the transition front, with frequency $\omega_0 = v k_f$. The wavenumber k_f corresponds to the feeding waves that cause the failure to propagate with constant speed v. Following [15], this allows one to rewrite the right-hand side of (23) as

$$\frac{1}{L_+(k)\Psi_+(k)}w_+ + \frac{L_-(k)}{\Psi_-(k)}w_- = \left[\frac{Ce^{\mathrm{i}\phi}}{0 - \mathrm{i}(k - k_f)} + \frac{\overline{C}e^{-\mathrm{i}\phi}}{0 - \mathrm{i}(k + k_f)}\right.$$
$$\left. + \frac{Ce^{\mathrm{i}\phi}}{0 + \mathrm{i}(k - k_f)} + \frac{\overline{C}e^{-\mathrm{i}\phi}}{0 + \mathrm{i}(k + k_f)}\right], \tag{24}$$

where ϕ is the phase of the feeding wave and C is a constant to be linked to the amplitude of the feeding wave. The solution to the above equation is then found in the form

$$w_+ = L_+(k)\Psi_+(k)\left[\frac{Ce^{\mathrm{i}\phi}}{0 - \mathrm{i}(k - k_f)} + \frac{\overline{C}e^{-\mathrm{i}\phi}}{0 - \mathrm{i}(k + k_f)}\right], \tag{25}$$

$$w_- = \frac{\Psi_-(k)}{L_-(k)}\left[\frac{Ce^{\mathrm{i}\phi}}{0 + \mathrm{i}(k - k_f)} + \frac{\overline{C}e^{-\mathrm{i}\phi}}{0 + \mathrm{i}(k + k_f)}\right]. \tag{26}$$

4.2 The fracture criterion and uniqueness of the solution

In terms of the the moving coordinate system, the condition (1) can be re-interpreted for the steady-state failure process as

$$w(0) = w_c, \quad \text{and} \quad w'(+0) < 0. \tag{27}$$

The first of these conditions can be satisfied by computing the limits

$$w(\eta)\big|_{\eta=0} = \lim_{k \to \mathrm{i}\infty} -\mathrm{i}k\, w_+ = \lim_{k \to -\mathrm{i}\infty} \mathrm{i}k\, w_- \tag{28}$$

using (25) and (26). In doing this we obtain

$$w_c = 2\mathrm{Re}(Ce^{\mathrm{i}\phi}), \tag{29}$$

which allows for the determination of ϕ if the feeding wave amplitude, and consequently C, are known. With regard to the second condition in (27), we construct the asymptote of w_+ in (25) as $k \to \mathrm{i}\infty$. We have

$$w_+ = \frac{2\mathrm{Re}(Ce^{\phi})}{\mathrm{i}k} - \frac{1}{k^2}\left[\mathrm{Im}(Ce^{\mathrm{i}\phi}) + \mathrm{Re}(Ce^{\mathrm{i}\phi})\left\{2(b - l) + \frac{1}{\pi}\int_{-\infty}^{\infty}\ln L(\xi)d\xi\right\}\right] + O\left(\frac{1}{k^3}\right)$$

for $k \to \mathrm{i}\infty$. Owing to the fact that

$$\int_0^{\infty}\eta e^{\mathrm{i}k\eta}dk = \frac{1}{(0 + \mathrm{i}k)^2},$$

we obtain that the second condition in (27) is satisfied if

$$\mathrm{Im}(Ce^{\mathrm{i}\phi}) + \mathrm{Re}(Ce^{\mathrm{i}\phi})\left\{2(b - l) + \frac{1}{\pi}\int_{-\infty}^{\infty}\ln L(\xi)d\xi\right\} < 0, \tag{30}$$

The proceeding allows for ϕ to be uniquely determined as a solution of (29).

5 Dynamic loading and features of the flexural structure during the steady-state fracture regimes

We discuss the dynamic behaviour of the structure, subjected to a sinusoidal load, during the alternating generalised strain failure process.

5.1 Sinusoidal remote load and expression for the feeding wave

We assume a sinusoidal load acts at some point far from the origin on the negative x-direction (see Figure 2). inside the structure. The load has amplitude $\mathcal{P}_0$ and frequency ω_0. Following the normalisations adopted in Section 2.3, we introduce the normalised forms of these quantities as

$$\omega = \sqrt{\frac{Ma^3}{E_1 J_1}}\omega_0 , \quad P = \sqrt{\frac{a^2}{E_1 J_1}}\mathcal{P}_0 .$$

This load generates a wave incident on the moving interface with the form

$$w_f(\eta) = \frac{P}{2k_f R_0(k_f, \omega)} \cos(k_f \eta - \phi) . \tag{31}$$

where ϕ is the feeding wave phase and

$$R_0(k, \omega) = \frac{h_2(k, \mathrm{i}\omega)}{(0 - \mathrm{i}(k - k_f))(0 + \mathrm{i}(k - k_f))} , \tag{32}$$

(see the Appendix for the derivation of the amplitude in (31)).

Next, we determine the expression of the constant C in the solution (25), (26) by considering the fracture criterion at the point $\eta = 0$. We note that the the form of the feeding wave based on (31) can be retrieved if one considers the complex residues of the simple poles at $k = \pm k_f$ for the inverse Fourier transform of w_-. This is derived under the assumption $\eta \to -\infty$, corresponding to a remote distance far behind the transition front and using

$$\frac{1}{2\pi} \int_{-\infty}^{\infty} w_-(k) e^{-\mathrm{i}k\eta} dk . \tag{33}$$

In doing so, we have

$$w_f = \left[\frac{\Psi_-(k_f)}{L_-(k_f)} C e^{\mathrm{i}(\phi - k_f \eta)} + \frac{\Psi_-(-k_f)}{L_-(-k_f)} \overline{C} e^{-\mathrm{i}(\phi - k_f \eta)} \right] \tag{34}$$

Noting that

$$\Psi_\pm(-k) = \overline{\Psi_\pm(k)}, \quad L_\pm(-k) = \overline{L_\pm(k)} ,$$

we obtain

$$w_f = 2\mathrm{Re}\left[\frac{\Psi_-(k_f)}{L_-(k_f)} C e^{\mathrm{i}(\phi - k_f \eta)} \right] . \tag{35}$$

Comparing with (31), we see that

$$C = \frac{L_-(k_f) P}{4 k_f R_0(k_f, \omega) \Psi_-(k_f)} . \tag{36}$$

11

5.2 Criterion for steady-state failure propagation in the alternating generalised strain regime

For the crack to propagate steadily with speed V, it is required that for $t = a/V$ ($\eta = 0$)

$$|w_f(\eta)| > w_c \ .$$

Using this condition (29) and (36), yields the criterion

$$\mathcal{P} \geq \mathcal{P}_{\min} \tag{37}$$

for the failure to propagate steadily in the alternating generalised strain regime, where

$$\mathcal{P} = P/w_c \qquad \text{and} \qquad \mathcal{P}_{\min} := \min \mathcal{P} = \frac{2k_f R_0(k_f, \omega)|\Psi_-(k_f)|}{|L_-(k_f)|} \ . \tag{38}$$

Figure 4, shows the plot of $\mathcal{P}_{\min}$ in (38) for a representative range of load frequencies. The computations are performed for $r = 0.4$, corresponding to a structure with soft supports, which will be investigated further in Section 6. For a given choice of the load frequency, the function plotted in Figure 4 predicts the $\mathcal{P}_{\min}$ required for a fracture process with speed $v = \omega/k_f$ to propagate through the flexural system. Here k_f is determined from the dispersion diagram. The grey solid curve corresponds to regimes with a higher fracture speed than those associated with the grey dashed curve. These curves are associated with the $\mathcal{P}_{\min}$ for the alternating generalised strain regime.

For illustrative purposes, we also plot the results of [25, 26] with black curves, that predict the appearance of pure steady-state modes, where the sign of the bending moments and shear forces are uniform at each instant of the failure process.

Accompanying these analytical computations is a verification of the predictions based on numerical simulations for a sufficiently large finite structure implemented in MATLAB (and described in detail in Section 6). There is a excellent agreement between the theoretical findings and the numerical computations.

5.3 Dynamic features for the alternating generalised strain regime

5.3.1 Reflected waves behind the transition front

The reflected waves can be derived from the residues of the poles $k = \pm z_{2j-1} + \mathrm{i}0$, $1 \leq j \leq l$, of the function w_-. The functions $w_r^{(s)}$, $1 \leq s \leq l$, representing the reflected waves, have the following form

$$w_r^{(s)} = A_r^{(s)} \cos(z_{2s-1}\eta - \psi_r^{(s)}) \ ,$$

with amplitude A_r^s given by

$$A_r^s = \frac{4|C||\Psi_-^r(z_{2s-1})|}{|L_-(z_{2s-1})||z_{2s-1}^2 - k_f^2|} \sqrt{z_{2s-1}^2 \cos^2(\phi + \psi_c) + k_f^2 \sin^2(\phi + \psi_c)}$$

where

$$\Psi_-^r(z_{2s-1}) = \frac{(-1)^{b-l}(1 + \mathrm{i}z_{2s-1})^{2(l-b)}}{2\mathrm{i}z_{2s-1}} \frac{\displaystyle\prod_{j=0}^{b}(z_{2s-1}^2 - y_{2j-1}^2)}{\displaystyle\prod_{\substack{1 \leq i \leq l \\ i \neq s}}(z_{2s-1}^2 - z_{2i-1}^2)} \ ,$$

and the phase shift $\psi_r^{(s)}$ given as

$$\psi_r^{(s)} = \arg\left(-\frac{\mathrm{i}\Psi_-^r(z_{2s-1})(z_{2s-1}\cos(\phi + \psi_c) + \mathrm{i}k_f \sin(\phi + \psi_c))}{(z_{2s-1}^2 - k_f^2)L_-(z_{2s-1})}\right) \ , \quad \psi_c^{(j)} = \arg(C) \ .$$
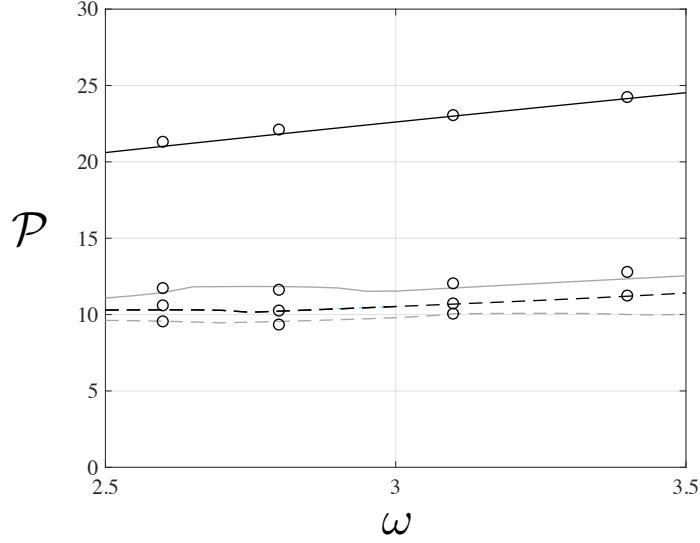
Figure 4: The plot of $\mathcal{P}_{\min}$ in a typical range of loading frequencies ω. Black curves are associated with the pure steady-state regimes identified in [25, 26] and the grey curves are computed using (37). The circles are results obtained form numerical simulations discussed in Section 6, where a sufficiently large system loaded by a sinusoidal load is considered and demonstrate what failure regimes can exist.

5.3.2 Waves transmitted ahead of the transition front

The waves that are transmitted ahead of the propagating interface are associated with the poles of the function w_+, at the points $k = y_{2j} - \mathrm{i}0$, $1 \le j \le b$.

The transmitted waves $w_{tr}^{(s)}$, $1 \le s \le b$, are given by:

$$w_{tr}^{(s)} = A_{tr}^{(s)} \cos(y_{2s}\eta - \psi_{tr}^{(s)}) \, .$$

Here the amplitude A_{tr}^s has the form

$$A_{tr}^s = \frac{4|C||\Psi_+^{tr}(y_{2s})||L_+(y_{2s})|}{|y_{2s}^2 - k_f^2|} \sqrt{y_{2s}^2 \cos^2(\phi + \psi_c) + k_f^2 \sin^2(\phi + \psi_c)}$$

with

$$\Psi_+^{tr}(y_{2s}) = \frac{(-1)^{l-b}}{2\mathrm{i}y_{2s}(1 - \mathrm{i}y_{2s})^{2(l-b)}} \frac{\displaystyle\prod_{j=1}^{l}(y_{2s}^2 - z_{2j}^2)}{\displaystyle\prod_{\substack{1 \le i \le b \\ i \ne s}}(y_{2s}^2 - y_{2i}^2)} \, .$$

The phase shift $\psi_r^{(s)}$ is

$$\psi_r^{(s)} = \arg\left(\frac{\mathrm{i}\Psi_+^{tr}(y_{2s})L_+(y_{2s})[y_{2s}\cos(\phi + \psi_c) + \mathrm{i}k_f \sin(\phi + \psi_c)]}{y_{2s}^2 - k_f^2}\right) \, .$$

6   Numerical simulations modelling the failure process

In this section, we implement a numerical scheme in MATLAB that models the behaviour of a finite flexural structure subjected to a sinusoidal load. In addition, using the numerical scheme we also trace the propagation of failure inside this structure as a result of the action of the load.

We use the results concerning the alternating generalised strain fracture regime within the flexural structure, presented in Section 2, to show that we can predict: (i) when such regimes occur, (ii) the speed with which the fracture propagates in such regimes and (iii) the behaviour of the structure in these particular regimes.

6.1   Geometry in the numerical model

A finite structure composed of 3800 nodes, connected by massless beams, is considered. These beams have length equal to unity. The position of each mass is given by $x = n$, $1 \leq n \leq 3800$. The system is initially at rest.

As in the previous sections, we consider this structure composed of an supported region and a region where the masses along the central axis of the structure are unsupported by such links. In what follows, the latter region will be referred to as the unsupported part of the structure.

The nodes corresponding to $0 \leq x \leq 1999$ constitute the unsupported part of the structure, behind the interface, and the remaining 1800 nodes (corresponding to $2000 < x \leq 3800$) represent the system in the supported region. Therefore, the interface between these two media is initially at $n = 2000$.

The external applied force is taken as an sinusoidal force having the form $P \sin(\hat{\omega} t)$, where P is the amplitude and $\hat{\omega}$ is the frequency of the load. This load is situated at node $x = 1800$. We can choose the value of $\hat{\omega}$ based on the frequency ω of the unforced problem of infinite extent considered in the previous sections. As mentioned in Section 5.1, this force creates the feeding waves that help to initiate and propagate the failure process.

Fracture regimes in two different types of structure are examined here:

1. Case 1 (see Section 6.2): Here, $r = 0.4$ that represents a structure whose supporting transverse links are "softer" than those along the central axis of the structure and

2. Case 2 (see Section 6.3): When $r = 3.4$, representing the structure with transverse supports that are much stiffer than the beams along its central axis.

6.2   Case 1

Here we show that it is possible to encounter two fracture regimes. The first involves the regime where the fracture criterion (1) could be fulfilled. The second concerns the regime defined by

$$w_j(t) < w_c, \quad j \geq p, \quad p, j \in \mathbb{Z} , \tag{39}$$

where p represents the node number where the interface is located at a given time t. This was studied in detail in [25, 26]. For these regimes, the sign of the generalised strains at the instant of each fracture in the structure remains constant. We refer to these regimes as the *pure steady-state regimes*.

We first show that speeds associated with the failure regimes observed can be predicted from the dispersion curves (16), (17) and those identified in [25, 26].
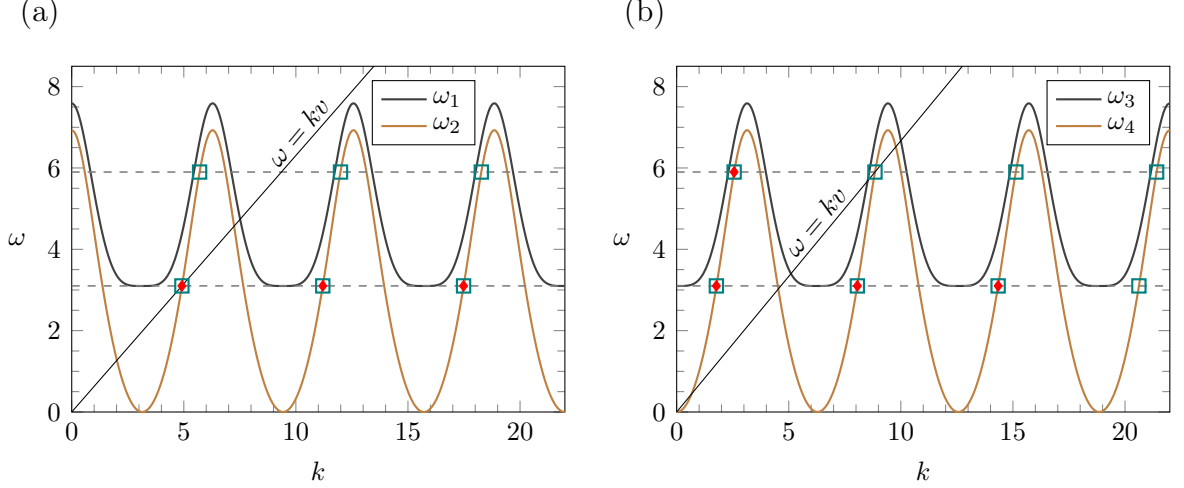
Figure 5: Dispersion relations plotted as functions of the wavenumber k for $r = 0.4$. In (a) and (b) the considered load frequencies $\omega = 3.1$ and 5.9 are shown as dashed horizontal lines. The squares represent the intersection points the curves with these lines. In (a), the dispersion curves are for the case of the alternating generalised strain regime for fracture propagation (see (16) and (17)). In (b), the relations ω_3 and ω_4 correspond to pure steady-state regimes where conditions (39) are applicable (see [25, 26]). The slope of the ray $\omega = kv$ that passes through the intersection points indicates possible steady-state speeds. Those intersection points with the red diamonds are associated with failure regimes observed in the numerical simulations.

6.2.1 Predicting failure speeds

A list of steady-state speeds for the considered fracture regimes can be determined using the dispersion curves discussed in Section 3. Figure 5(a) shows the dispersion curves (16), (17) plotted as functions of the wavenumber k for the case $r = 0.4$. In addition, the horizontal dashed lines represent the loading frequencies.

For the case $\omega = 3.1$, the horizontal dashed line in Figures 5(a) and (b) associated with this frequency intersects the curves given by $\omega_2(k)$ and $\omega_4(k)$ infinitely many times. Since we require a feeding wave to reach the transition front inside the structure, we need the group velocity v_g of this wave to be greater than the fracture speed v that is slope of the line $\omega = kv$. For $k > 0$, we have indicated using squares the intersection points, representing possible feeding waves, where this criterion is satisfied in Figure 5(a) and (b).

Without loss of generality, we take the first of these points (k^*, ω^*), with the smallest wavenumber, along the line $\omega = 3.1$. We connect this point to the origin by a ray whose slope is defined by $v = \omega^*/k^*$ (see Figure 5(a)). This slope predicts a possible steady-state speed of failure inside the structure. In the case of $\omega = 3.1$ in Figure 5(a), such an intersection point is given by $(k^*, \omega^*) = (4.915, 3.1)$ and the slope of the corresponding ray is 0.6307. That particular intersection point corresponds to an alternating generalised strain failure regime with speed $v = 0.6307$ initiated by the sinusoidal load of frequency $\omega = 3.1$.

Owing to the 2π-periodicity of the function $\omega_2(k)$, a decreasing sequence of possible speeds can be deduced in the form

$$v = \frac{\omega^*}{k^* + 2\pi n}, \quad n \geq 0, n \in \mathbb{Z}.$$
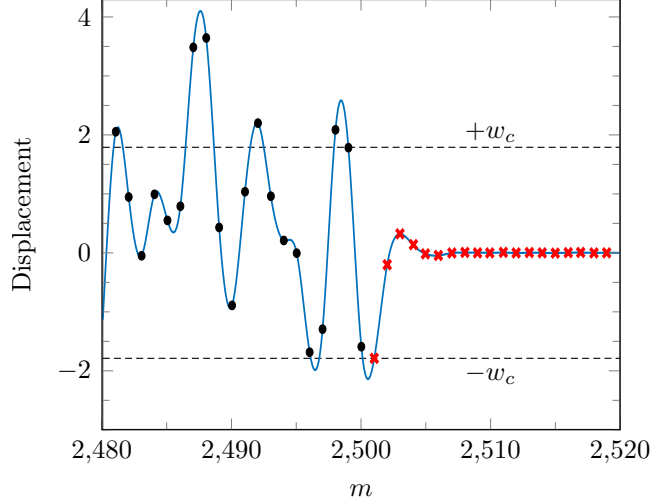
15

Figure 6: Displacement profile attained by the central axis of the harmonically excited flexural system that is undergoing a steady failure with the alternating generalised strain mode. The frequency and amplitude of the external load is $\omega = 3.1$ and $\mathcal{P} = 13.115$, respectively. The speed of failure for this particular regime is $v = 0.6307$. Masses along the unsupported structure are represented by black dots and those masses supported by transverse links are marked with crosses. The limits $\pm w_c$, with $w_c = 1.7919$, of the critical displacement for every mass in the supported region is indicated by horizontal dashed lines. The video of the Supplementary Material shows the evolution of the failure process and the behaviour of the structure from the transient analysis undertaken here.

As an example, for the case $\omega = 3.1$ in Figure 5(a), this list takes the form

$$v = 0.6307,\ 0.2768,\ 0.1773,\ 0.1304,\ 0.1302,\ ... . \tag{40}$$

The intersection points connected with these speeds are shown along the line defined by $\omega = 3.1$ in Figure 5(a).

In the numerical simulations we can also identify pure steady-state regimes corresponding to the case when the conditions for the failure propagation (39) are applicable. In this case, following [25, 26], the dispersion relations are given by $\omega_{j+2}(k) = \Omega_j(k)$, $j = 1, 2$, (see (14)) and are shown in Figure 5(b). Repeating the procedure outlined above, we can obtain the speeds in the pure steady-state regime. For $\omega = 3.1$, the list of predicted speeds for this regime is:

$$v = 1.7484,\ 0.3848,\ 0.2162,\ 0.1503,\ 0.1152,\ ... .$$

Predictions for the potential steady-state speeds at different load frequencies can be calculated in a similar way.

6.2.2 Soft supports and a typical loading frequency in the pass band

In this example, we set $r = 0.4$ and $\omega = 3.1$, and analyse the failure processes in the finite structure for various load amplitudes.

Transient analysis of the alternating generalised strain failure regime

The video in the Supplementary Material shows the dynamic behaviour of the structure subjected to the oscillating load with amplitude $\mathcal{P} = 13.115$. Here, the steady-state propagation occurs with

16

the speed $v = 0.6307$. In this particular regime, one observes the occurrence of fracture in the supported part whenever the displacement of ± 1.7919 is reached. Note that within the steady-state regime, between each breakage, the sign of the mass displacements alternate.

On the left-hand frame of the video, a global view of the structure is provided where the position of the point force is also indicated. The magenta rectangle highlights a neighbourhood of the transition front, and the magnification of this rectangle is shown to the right panel of the video. There, the horizontal lines depicting the critical values of the displacement are indicated. Each time a mass inside the supported region reaches one of the values, ± 1.7919 and the blue circle representing the mass is removed. The corresponding physical process is the breakage of the transverse links in the supported part at that time instant and position.

The applied load produces elastic waves, which excite the structure. Initially, the force causes the masses in the unsupported region to oscillate and this force generates waves propagating towards the interface, positioned at the 2800th mass. At approximately $t = 9$s, the mass at the interface starts to oscillate within the limits defined by the critical displacement and the first breakage is achieved at $t = 11$s. This occurs when the smallest critical value of displacement of -1.7919 is reached. After this time we see the transition front propagate through the structure. As we will see later, the initial stage of this process is generally non-steady.

FOR SUPPLEMENTARY MATERIAL(?): At approximately $t = 2$min 40s, the steady propagation of the transition front with speed 0.6307 is reached. Before this instant, transient waves with significant amplitude are transmitted into the supported region. The amplitude of these transmission waves diminishes until the steady-state fracture regime is achieved. We note within the particular steady-state regime shown in the video, no waves are transmitted into the supported part of the structure. Behind the transition front, one can find the superposition of the feeding wave and a single wave reflected by the transition front. Here, as we show below, the dynamic features of the structure can predicted using the theory in Sections 2–4.

Dependency of the average failure speed on the load amplitude

We observe six speeds with which the transition front can propagate steadily. These include the speeds $v = 0.1773, 0.2768, 0.6307$, which correspond to alternating generalised strain regimes, and $v = 0.2162, 0.3848, 1.7484$ that are the speeds associated with the pure steady-state regimes.

In the Figure 7, we show the average fracture speed $\bar{v}$ as a function of the normalised oscillating force amplitude $\mathcal{P}$. We note the index of the mass and the time failure occurs in each simulation (examples of this are shown in Figure 9(a) for various steady-state regimes). The average speed $\bar{v}$ is then computed as the slope of the line of best fit for this data. Figure 7 shows the average steady-state speed $\bar{v}$ and from this we can conclude:

- The average speed is a monotonically increasing function of the load amplitude.

- There also exists several plateaus, highlighted in red and blue indicating alternating generalised strain regimes and pure steady-state regimes, respectively, where theoretical speeds are realised.

- Only a finite collection of theoretically predicted speeds are realised, where lower speeds exist for narrow intervals of the load amplitude or are never realised.

- Between any two pure steady-state regimes, corresponding to the fracture process defined by criteria (1), there exists a plateau of finite width at the failure speed associated with the alternating generalised strain failure regime.
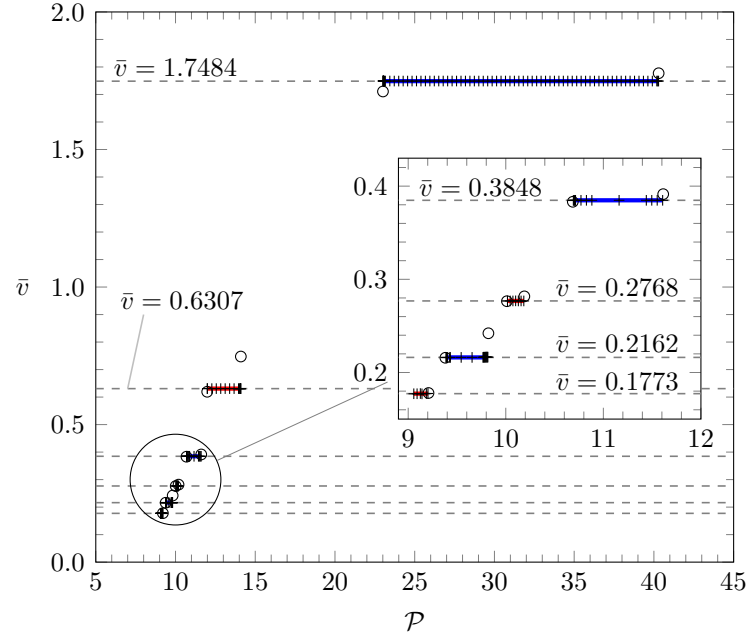
Figure 7: The average failure speed shown as a function of the quantity $\mathcal{P} = P/w_c$, for $\omega = 3.1$ and $r = 0.4$. The circles and crosses represent the fracture behaviour for different regimes recorded from the numerical model. Specifically, the crosses are associated with the steady-state propagation of the transition front and the circles indicate non steady-state propagation regimes. The dashed horizontal lines are for the predicted steady-state speeds that follow from from the dispersion curve analysis in Section 6.2.1. Here, the plateaus for the steady-state speeds are shown as red for the alternating generalised strain regimes and blue for the pure steady-state regimes.

Average Speed	Initial Force Amplitude		Regime
	Numerical Value	Theoretical Value	
0.1773	8.985	8.932	1
0.2162	9.376	9.366	2
0.2768	10.045	10.055	1
0.3848	10.715	10.686	2
0.6307	11.887	11.742	1
1.7484	23.048	23.00	2

Table 1: Load amplitude values that initiate steady-state failure regimes for $\omega = 3.1$ and $r = 0.4$. The first column is the average speed obtained from the numerical scheme. The second column presents the numerical values for the load amplitude where the particular steady failure regime was observed. This is also accompanied by the theoretical predictions based the results of Section 4 and the theory of [25, 26]. In the last column we also specify the regime encountered, where "1" represents the alternating generalised strain regime and "2" indicates the pure steady-state regime.

- The size of plateaus for each steady-state regime corresponding to the alternating generalised strain fracture process increases with the load amplitude. The same behaviour is observed for the plateaus corresponding to the pure steady-state regimes.

- Outside of the plateaus, the fracture propagates non-uniformly. Between two steady-state speeds, we encounter the clustering phenomenon, first encountered in [9], where fracture propagates in regular periodic bursts.

These conclusions can also be generalised to different r and ω values as we will see.

Additionally, in correspondence with Section 5, we show that the theory can be used to efficiently predict the initial load amplitudes for when steady-state failure regimes can appear. In Table 1, we present data from the simulations for when the steady-state regimes are initiated and we supply the classification of each regime. The theoretical predictions for these load amplitudes, based on the right-hand side of (37) and the results of [25, 26], are also given. We note there is an excellent match between the theoretical results and the numerical results in Table 1.

Behaviour of the system during the dynamic failure process

For $\mathcal{P} = 13.115$, Figure 8(a) shows the system undergoing failure at a particular time $t = 1012.4$s after the fracture of 600 pairs of transverse links. The failure here propagates steadily under the alternating generalised strain regime with speed $v = 0.6307$. In this case, one can observe the combination of the feeding and reflected waves behind the transition front. Ahead of this point, there exists an evanescent wave. We note that at the next time instant ($t = 1012.4 + 1/v$) when the failure occurs, the profile of the structure can be obtained that shown in Figure 8(a) mirrored about a horizontal line that corresponds to zero displacement. In Figure 8(b), we consider the pure steady-state regime for an external load amplitude $\mathcal{P} = 33.484$ is applied. The time corresponding to when the snapshot is taken at $t = 403$s. The achieved steady-state speed is $v = 1.7490$ and as the failure propagates steadily, the profile of the structure local to the transition front is preserved. Figure 8(b) is an example of the pure steady-state regimes studied in [25, 26] that also occur in the simulations presented here.

In both Figures 8(a) and 8(b), we compare numerical data for the arrangement of the masses along the profiles with the theoretical results of Section 4 and [25, 26]. Here, for the theoretical
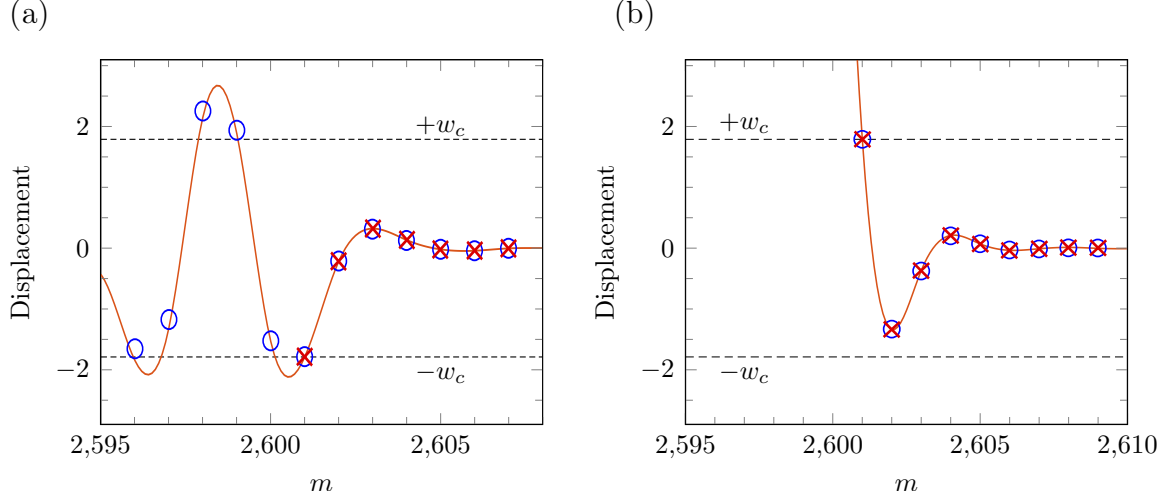
Figure 8: Here we present the snapshots of the transition front steadily propagating, with two different regimes, through the structure excited by a harmonic load of frequency $\omega = 3.1$. In (a) the snapshot is taken at $t = 1012.4$s for $\mathcal{P} = 13.115$ and the alternating generalised strain regime propagates with speed $v = 0.6307$. In (b) $t = 403$s with $\mathcal{P} = 33.484$ and this corresponds to a pure steady-state speed of $v = 1.7484$. The blue circles in each panel are based on the theoretical results presented in Section 4 and represent the mass displacements. The profile shown is determined from the MATLAB simulations, where the crosses are the masses situated in the supported region.

computations in Figure 8(a) the inverse Fourier transform of (25) and (26) is computed using (36), ensuring that (30) holds for the feeding wave phase determined from (29). For the computations in Figure 8(b), the same procedure is followed based on the results of [25, 26]. We emphasise there is again an excellent agreement between the numerical and theoretical results.

Behaviour of the transition front in time

By analysing the position of failure in the supported region as a function of time we can get a better understanding of how the transition front behaves during the failure process. In Figure 9(a), this is shown for a range of load amplitudes situated inside the plateaus observed in Figure 7 corresponding to the alternating generalised strain regimes. We remark that as the transient simulations have been used to obtain this data, we can expect some effects in the initial period of the failure process. For instance, for $\mathcal{P} = 11.496$ in Figure 9(b) we see a visible oscillatory behaviour in the transition front speed initially. After this initial period, the transition process settles and the steady-state failure phenomenon is achieved.

Actually, one can observe further oscillations in the failure speed when it appears to have settled to a uniform state. We define the instantaneous speed v_i for the fracture process as

$$v_i = \frac{m_i - m_{i-1}}{t_i - t_{i-1}}, \text{ if } i \geq 2 \,. \tag{41}$$

where m_i is the position of fracture and t_i the time at which this occurs. Using the notion of the instantaneous speed, we also can understand how quickly the failure process settles to the steady-state limit.

In Figure 9(c), we show the instantaneous speed plotted as function of the failure position m_i. Here, instantaneous speed data corresponds to several cases considered in Figures 9(a) and (b). To
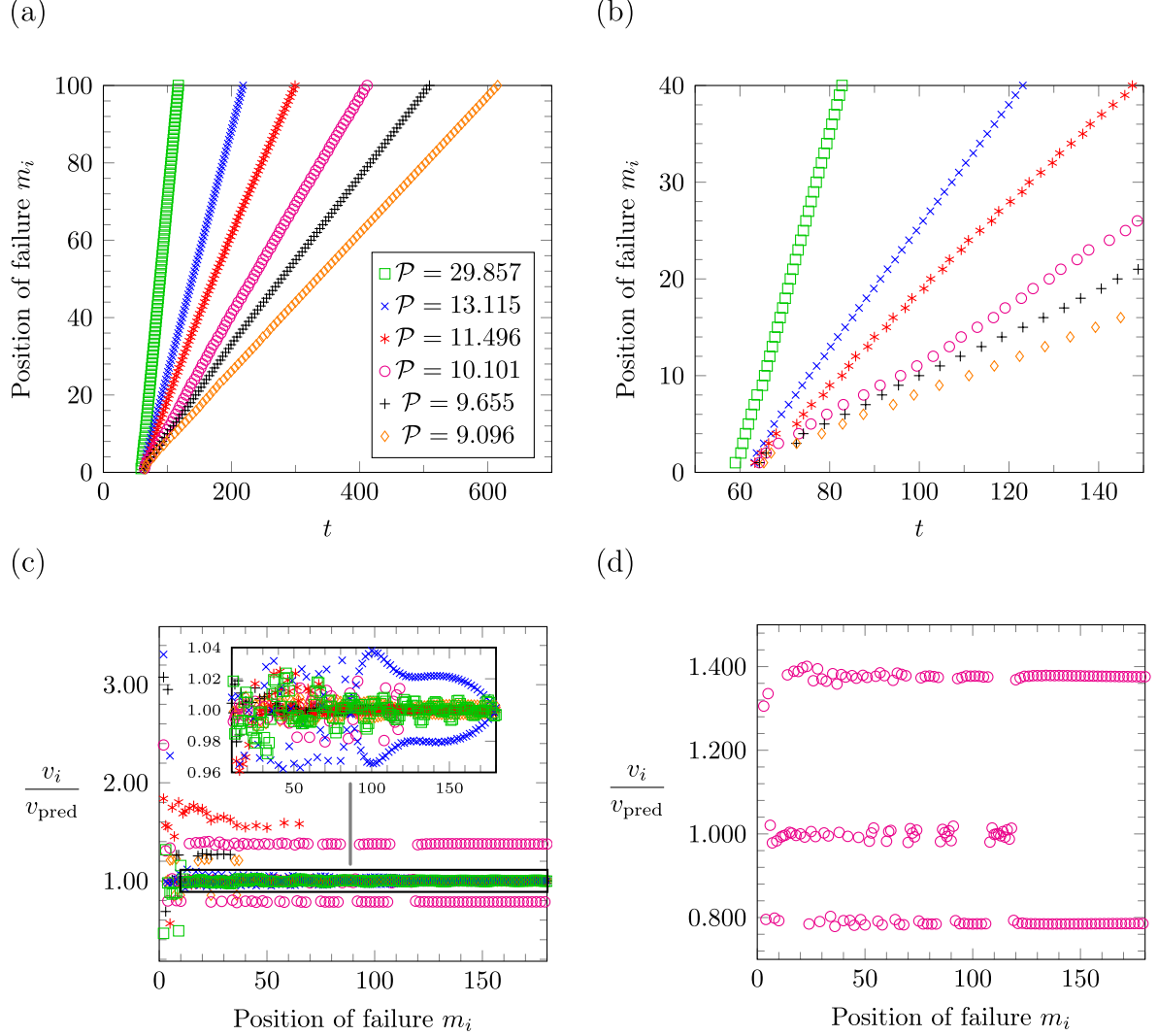
20

Figure 9: For $r = 0.4$ and $\omega = 3.1$ here we show the behaviour of the transition front as a function of time for various load amplitudes $\mathcal{P}$. (a) The position of failure inside the supported part of the structure as a function of time. (b) A magnification of the the initial data of the computations in (a). (c) The normalised instantaneous speeds computed via (41) (and normalised by the respective predicted steady-state speeds based on the dispersion diagrams in Section 3). The key for the data presented is given in the inset of (a).

demonstrate the speed of convergence to the steady-state failure process, each set of data has been normalised by the corresponding theoretical speed. In this case, convergence to the steady-state speed is represented by the convergence to unity in Figure 9(c). It is observed that the instantaneous speeds, for nearly all the load amplitudes, oscillate about the predicted speed in each case (see the magnification on the inset of Figure 9(c)). In fact, the inset of Figure 9(c) shows that there exist micro-oscillations in speed of the failure front not necessarily seen in Figures 9(a) and (b). In addition, these oscillations are not incorporated in the assumptions of the theoretical model studied in Section 2–5. Larger oscillations in the transition front speed are attained with larger values of the amplitude $\mathcal{P}$. The speed of convergence of these regimes appears to be a non-monotonic function of the load amplitude.

Further, in Figure 9(d), we show a special case ($\mathcal{P} = 10.101$) where the instantaneous speed of the front does not converge to unity in the steady failure process, but instead settles to two distinct speeds (given by v_i/v_{pred} approximately equal to 0.79 and 1.39 after the 118th failure event). Although there is an apparent jump in the instantaneous speed of the failure, the average speed $\bar{v}$ is in fact equal to the predicted value ($v = 0.2768$). Moreover, the corresponding data representing the failure position as a function of time on Figure 9(a) exhibits a straight line that is commonly associated with the steady-state failure propagation.

6.2.3 Failure induced by a high frequency

Here, we give an example of when the alternating generalised strain regime is never realised. In this illustration, $\omega = 5.9$ and $r = 0.4$. As mentioned earlier in Section 6.2.1, the theoretical model predicts a semi-infinite list of possible speeds for both the alternating generalised strain regimes and the pure steady-state regimes (also see the dispersion curves Figure 5 with the intersection points for $\omega = 5.9$). However, we observe only one of the predicted steady-state speeds in the numerical simulations. Figure 10(a), shows the average speed $\bar{v}$ as a function of the point load amplitude $\mathcal{P}$. This particular regime identified is a pure steady-state regime and the failure speed is $v = 2.3020$. The load amplitude interval for where this regime is realised is $46.2172 \leq \mathcal{P} \leq 52.612$ and this is again in good agreement with the theoretical predictions of [25, 26].

In Figure 10(b), we show the position of failure within the supported region as a function of the time when $\mathcal{P} = 46.534$, $\mathcal{P} = 49.7$ and $\mathcal{P} = 51.282$. These values are located within interval defining the plateau for the pure steady-state failure process. For $\mathcal{P} = 46.534$, we see that the transition front speed is constant and equal to the predicted steady-state speed $v = 2.3020$, after approximately 44 breakages. Prior to this, the front propagates non-steadily in the transient regime. For $\mathcal{P} = 49.7$, the pure steady-state regime is reached earlier at approximately the 13-th breakage. On the other hand, for $\mathcal{P} = 51.282$, we see the failure inside the system settle to the steady-state regime after 100 breakages.

For the same amplitudes, in Figure 10(c), we present the instantaneous speed v_i, defined by (41), as a function of the position of fracture. The instantaneous speeds again oscillate about the theoretical speed. It is apparent from Figure 10(c) that for those load amplitudes, situated at the extremes of the plateau in Figure 10(a), the failure process will behave irregularly during large initial period of the failure process. For $\mathcal{P} = 49.700$ situated inside the plateau of Figure 10(a), the process is seen to converge to a more regular oscillatory behaviour earlier in the failure process.

6.3 Case 2

Here we analyse the failure process in a structure possessing transverse links that are "stiffer" than the links along the central axis of the structure
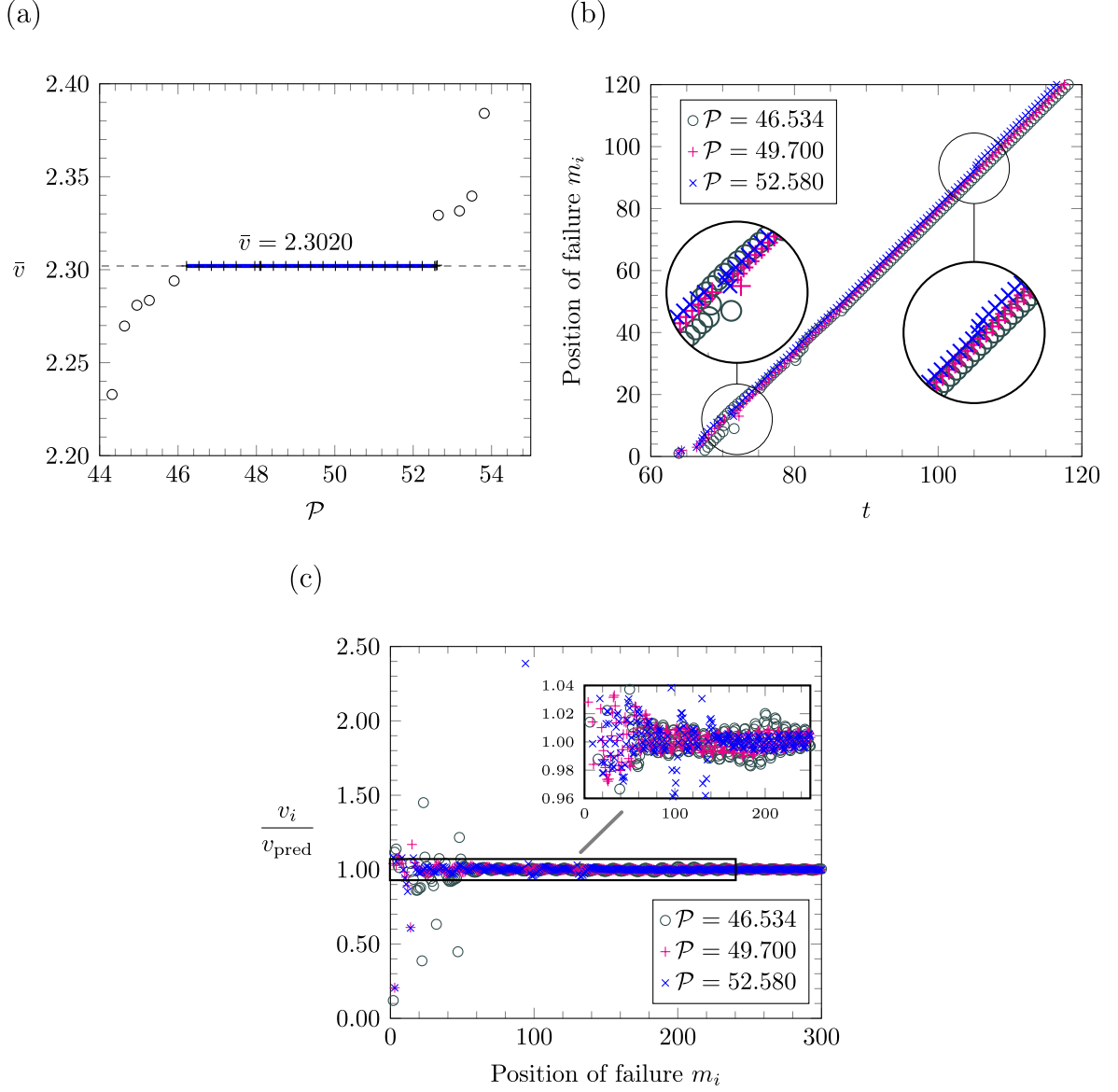
Figure 10: Failure regimes identified for $\omega = 5.9$ and $r = 0.4$. (a) The average failure speed is shown as a function of $\mathcal{P}$. For the description of this figure, we refer to Figure 7. In (b) we show the position of failure inside the supported part of the structure as a function of time. On the inset of (b), we present magnifications of the profiles where various non-steady propagation phenomena can be observed that is associated with transient failure process. (c) The normalised instantaneous speeds computed using (41) (that are normalised by the respective predicted steady-state speed based on the dispersion diagram, see Section 3) as a function of the failure position. The insets of (b) & (c) also contain the key for the computations.

6.3.1   Stiffer supports and intermediate load frequency

Now the supports in the system are characterised by $r = 3.4$. Here, we first study the case when this structure is subjected to an oscillating force with a frequency $\omega = 3.1$. Although the flexural stiffness of the transverse links inside the supported region is now larger compared to that of the beams along the central axis, the list of admissible steady-state speeds for failure, outlined in Section 6.2.1, remains the same. The numerical simulations described below indicate which of these regimes are realised.

We first recall the results of Section 6.2.2, where the same load frequency was considered and the structure was supported by transverse links with a lower flexural stiffness. There, it was possible to find several failure regimes (both alternating generalised strain regimes and pure steady-state regimes) with different speeds.

When $r = 3.4$, we only observe one of the predicted steady-state speeds, $v = 1.7484$, which corresponds to a pure steady-state regime with the highest possible speed. The regimes analysed in Sections 2-4 are not observed. In Figure 11(a), we show the average speed $\bar{v}$ as a function of $\mathcal{P}$. In comparing with the computations of Figure 7 for the case of a structure with softer supports, we note that the stiffer supports require larger load amplitudes that allow one to initiate and maintain the failure propagation, as expected. Moreover, the stiffer supports allow for a larger range of load amplitudes where the highest steady-state speeds can be observed (compare Figure 11(a) with Figure 7). The plateau in Figure 11(a) is defined by the interval $99.452 \leq \mathcal{P} \leq 211.972$, that agrees with the predictions based on the results in [25, 26].

Figure 11(b), shows the position of failure against time for $\mathcal{P} = 99.687, 195.62$ and 211.815, located in the interval defining the plateau for the steady regime. For the load amplitude $\mathcal{P} = 195.62$ the time interval for the initial transient failure process appears to be small and the steady-state regime is realised with speed $v = 1.7484$. For $\mathcal{P} = 99.687$, the transition front converges to the steady-state regime after approximately 27 breakages. For the largest amplitude $\mathcal{P} = 211.815$, the steady-state failure process is achieved approximately 48 breakages. It is interesting to note that for this larger load amplitude, the non-steady failure process attributed to the transient regime is visible and the profile propagates in steps that overlap (see inset of Figure 11(b)). This failure process is known as a forerunning fracture and was first identified for the problem of the separation of a beam from an elastic foundation when subjected to various loads [22].

In addition, the normalised instantaneous speeds v_i, calculated using (41), are shown in Figure 11(c) as a function of the failure position. These computations reveal large fluctuations in the transition front speed about the theoretical speed $v = 1.7484$, (represented by unity on the vertical axis in this figure). It is evident that the failure process corresponding to the load amplitudes $\mathcal{P} = 99.687$ and 211.815 (located at the extremes of the plateau in Figure 11(a)) give large fluctuations in the instantaneous speed of the transition front at the beginning of the failure process. After some time, for all cases shown, the instantaneous speeds oscillate about the predicted speed value in a regular manner and the amplitude of the oscillations decrease as the fracture process develops (see inset of Figure 11(c)).

The example presented here shows that the number of failure regimes observed for different structures subjected to a remote sinusoidal load with a fixed frequency can vary. In this case, the stiffer supports have reduced the number of possible failure regimes that are realisable.

6.3.2   High frequency loading of structure with stiff supports

Lastly, we consider a structure with sufficiently stiff supports and this structure is subjected to a sinusoidal load with a high frequency, which is located near the upper boundary of the passband
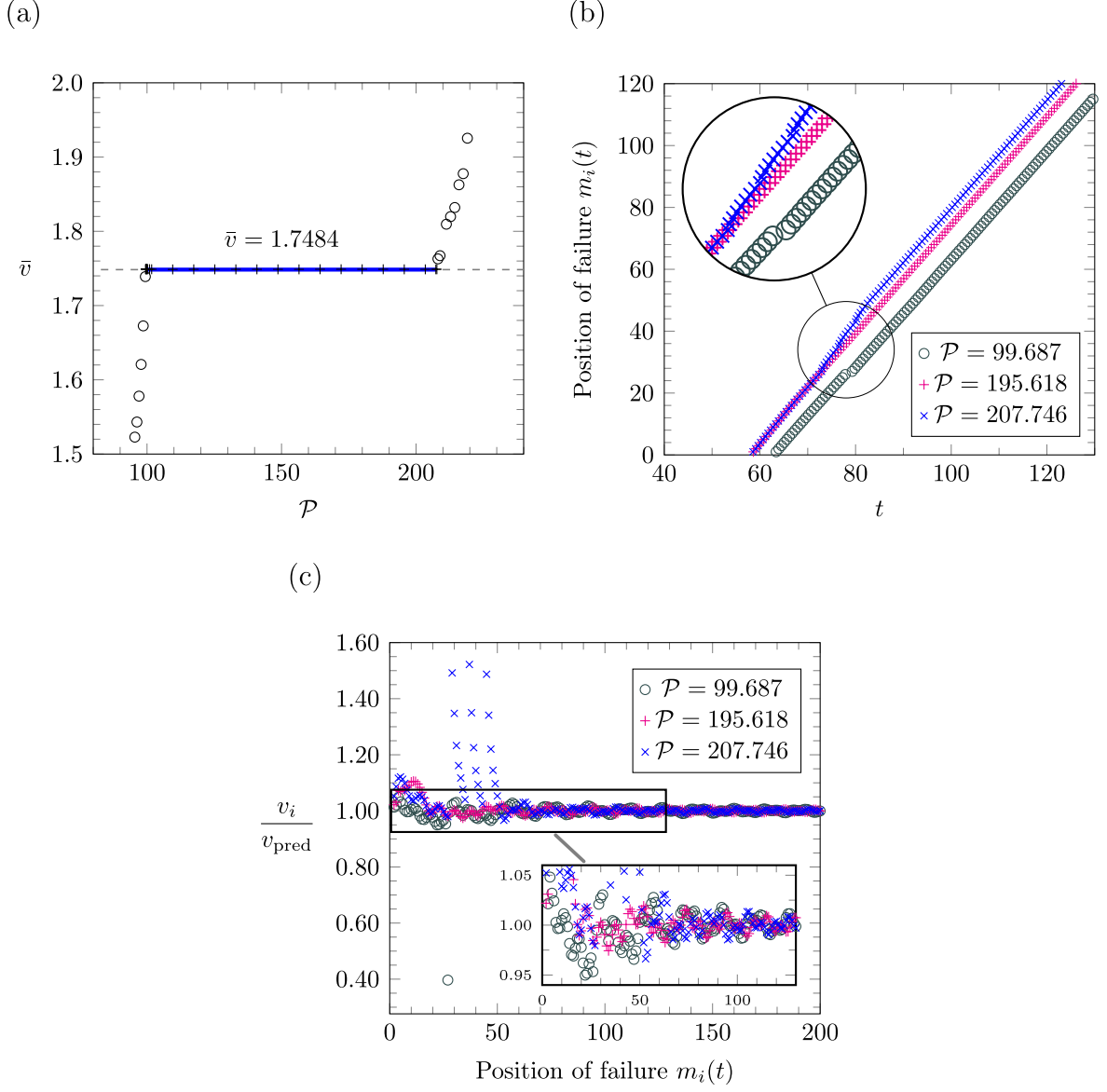
(a)

(b)

(c)

Figure 11: Computations for the failure process in structure with supports characterised by $r = 3.4$ subjected to a load with frequency $\omega = 3.1$. (a) The average failure speed shown as a function of $\mathcal{P}$ (see the Figure 7 for the description of the figure). In (b), we show the position of failure inside the supported part of the structure as a function of time. (a) The normalised instantaneous speeds based on (41) as a function of the position of failure. The legend for the computations in (b) & (c) is given in insets.
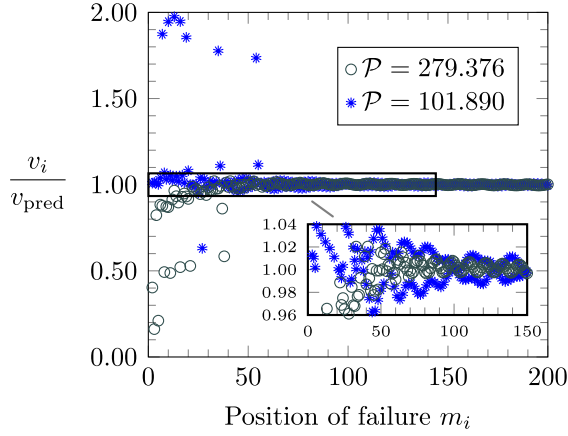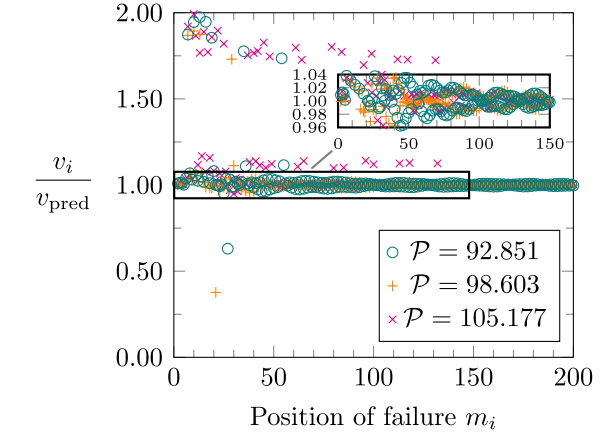
25
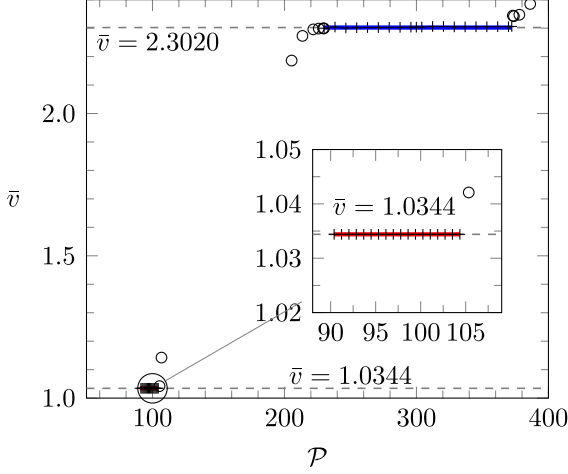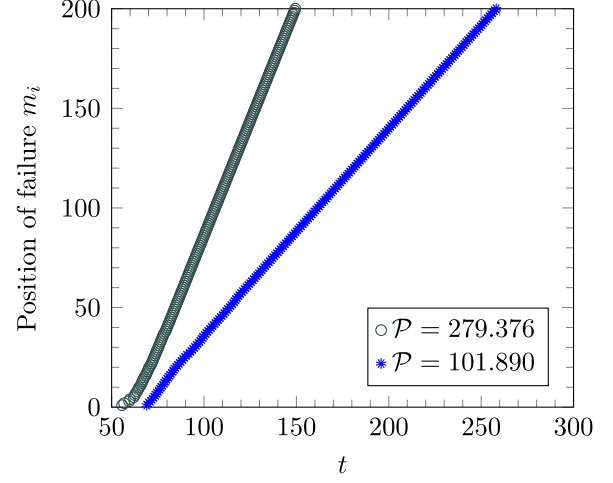
Figure 12: Results showing the behaviour of the transition front in the numerical simulations for $r = 3.4$ and $\omega = 5.9$. In (a), the average failure speed shown as a function of $\mathcal{P}$, is presented and the description of this figure can be found in Figure 7. In (b), we show the position of failure for load amplitudes corresponding to the alternating generalised strain regime and in (c) the associated instantaneous speed distributions are shown. The legend for the latter computations is in the inset of (b). For (b)–(d), the key for the computations are in the inset of these panels.

Figure 13: Computation for $r = 3.4$ and $\omega = 5.9$ when are applied the external load $\mathcal{P} = 101.890$ (results in blue circle marks) and $\mathcal{P} = 279.376$ (results in black cross marks). (a) shows the instantaneous speeds of the crack front. (b) The average transition front speeds as a function of $m* = 50$.

for unsupported part of the structure.

This particular example shows that the alternating generalised strain regime can be realised in high frequency regimes. In fact, the results of the numerical simulations show there are two regimes encountered, as shown in Figure 12(a). In this figure, it can be seen that plateaus exist for $90.386 \leq \mathcal{P} \leq 105.341$ and $230.074 \leq \mathcal{P} \leq 376.664$. These intervals again agree well with the theoretical predictions. The plateau there corresponding to the alternating generalised strain regime (with speed $v = 1.0344$) is very narrow in comparison to plateau belonging to the pure steady-state regime (having speed $v = 2.3020$). If we compare with the computations of Figure 9 for the same loading frequency, but for the structure with softer supports, we see the present configuration admits additional failure regimes at lower speeds.

Figure 12(b) shows how the position of failure varies as a function of time for load amplitudes chosen inside the lowest plateau of Figure 12(a) associated with the alternating generalised strain regime. The non-steady behaviour of the transition front in the transient regime is visible, and there exists visible variation on the failure speed. After this initial period, the system begins to settle to the steady-state failure process. The instantaneous speed distribution obtained using (41) for the cases analysed in Figure 12(b) is presented in Figure 12(c). It is again evident that there are large oscillations in failure speed about the theoretically predicted value in the initial period of the failure process. When the failure process settles, the instantaneous speeds follow a regular oscillatory pattern about the predicted speed. In this example, the computations for the pure steady-state regime ($\mathcal{P} = 279.376$) appear converge the fastest to the predicted speed (see inset of Figure 12(c)). Finally, we comment on the instantaneous speed distributions, shown in Figure 12(d), for some load amplitudes within the lowest plateau corresponding to the alternating generalised strain regime. The instantaneous speed associated with $\mathcal{P} = 92.851$ and $\mathcal{P} = 105.177$, at the extremes of the interval defining this plateau, clearly require a large duration of time to settle to the steady-state failure process with approximately the predicted speed. In fact in the case of $\mathcal{P} = 105.177$, several higher speeds are observed up to the 140th instant of failure. Following this, the instantaneous speed eventually settles into steady oscillations about the theoretically predicted speed for all cases shown in Figure 12(d).

7 Conclusions and discussion

Here, we have developed the analytical model characterising a particular propagation regime in a flexural system, composed of beams connecting periodically placed masses. The regime identified corresponds to the scenario where the generalised strains represented by bending moments and shear forces in the beam connections alternate in sign as the failure advances through the system.

Analytical results characterising the dynamics of the system during its failure and when possible failure regimes occur have been determined. In particular, the results have been shown to provide excellent predictions for the behaviour of sufficiently long finite systems subjected to sinusoidal loads modelled with independent numerical schemes. The numerical simulations revealed that the existence of regimes modelled here is dependent on the parameters governing structure and sinusoidal loading. In addition, these regimes are accompanied by those identified in [25, 26].

The model can be generalised to consider different types of loading and more complicated failure

criteria, where other types of special failure phenomena may exist. Applications of the tools developed here are envisaged in civil engineering, where the dynamics and failure of large multi-structures are considered.

References

[1] Marder, M. and Gross, S. (1995): *Origin of crack tip instabilities*, Journal of the Mechanics and Physics of Solids 43, no. 1, 1–48.

[2] Slepyan, L.I. (2001): *Feeding and dissipative waves in fracture and phase transition I. Some 1D structures and a square-cell lattice*, Journal of the Mechanics and Physics of Solids 49, 469–511.

[3] Slepyan, L.I. (2001): *Feeding and dissipative waves in fracture and phase transition II. Phase-transition waves*, Journal of the Mechanics and Physics of Solids 49, 513–550.

[4] Slepyan, L.I. (2001): *Feeding and dissipative waves in fracture and phase transition. III. Triangular-cell lattice*, Journal of the Mechanics and Physics of Solids 49, 2839?2875.

[5] Nieves, M.J., Movchan, A.B., Jones, I.S., Mishuris, G.S., (2013): *Propagation of Slepyan's crack in a non-uniform elastic lattice*, Journal of the Mechanics and Physics of Solids 61, no 6, 1464–1488.

[6] Slepyan, L.I. (2005): *Crack in a material-bond lattice*, Journal of the Mechanics and Physics of Solids 53, 1295–1313.

[7] Slepyan, L.I., Ayzenberg-Stepanenko, M.V. (2002): *Some surprising phenomena in weak-bond fracture of a triangular lattice*, Journal of the Mechanics and Physics of Solids 50, 1591–1625.

[8] Mishuris, G.S., Movchan, A.B. and Slepyan, L.I., (2007): *Waves and fracture in an inhomogeneous lattice structure*, Waves in Random and Complex Media 17, no. 4, 409–428.

[9] Mishuris, G.S., Movchan, A.B. and Slepyan, L.I., (2009): *Localised knife waves in structured in a structured interface*, Journal of the Mechanics and Physics of Solids 57, 1958–1979.

[10] Slepyan, L.I., Movchan, A.B., Mishuris, G.S., (2010): *Crack in a lattice waveguide*, International Journal of Fracture 162, 91–106.

[11] Mishuris, G.S., Movchan, A.B., Slepyan, L.I., (2008): *Dynamical extraction of a single chain from a discrete lattice*, Journal of the Mechanics and Physics of Solids 56, 487–495.

[12] Mishuris, G.S., Movchan, A.B., Slepyan, L.I., (2008): *Dynamics of a bridged crack in a discrete lattice*, Quarterly Journal of Mechanics and Applied Mathematics 61, no.2, 151–159.

[13] Gorbushin, N., Vitucci, G., Mishuris, G. and Volkov, G. (2017): *Influence of fracture criteria on dynamic fracture in discrete chain*, ArXiv preprint, arXiv:1704.08222v1.

[14] Marder, M. (1993): *Simple models of rapid fracture*, Physica D: Nonlinear Phenomena 66, no. 1: 125-134.

[15] Slepyan, L.I. (2002): *Models and Phenomena in Fracture Mechanics*, Foundations of Engineering Mechanics, Springer.

[16] Gorbushin, N. and Mishuris, G. (2017): *On admissible steady-state regimes of crack propagation in a square-cell lattice*, ArXiv preprint, arXiv:1701.04818v3.

[17] Gorbushin, N. and Mishuris, G., (2017): *Dynamic fracture of a discrete media under moving*, ArXiv preprint, arXiv:1701.02725v1.

[18] Gorbushin, N. and Mishuris, G., (2016): *Analysis of dynamic failure of the discrete chain structure with non-local interactions*, ArXiv preprint, arXiv:1512.01540v2.

[19] Ryvkin, M., Slepyan, L. (2010): *Crack in a 2D beam lattice: Analytical solutions for two bending modes*, Journal of the Mechanics and Physics of Solids 58, 902–917.

[20] Brun, M., Movchan, A.B. and Slepyan, L.I., (2013): *Transition wave in a supported heavy beam*, Journal of the Mechanics and Physics of Solids 61, no. 10, 2067–2085.

[21] Brun, M., Giaccu, G.F., Movchan, A., B., and Slepyan, L. I., (2014): *Transition wave in the collapse of the San Saba Bridge*, Front. Mater. 1:12. doi: 10.3389/fmats.2014.00012.

[22] Slepyan, L.I., Ayzenberg-Stepanenko, M.V., and Mishuris, G.S., (2015): *Forerunning mode transition in a continuous waveguide*, Journal of the Mechanics and Physics of Solids 78, 32-45.

[23] Marder, M., Deegan, R.D., Sharon, E., (2007): *Crumpling, buckling, and cracking: Elasticity of thin sheets*, Physics Today 60, no. 2, 33-38.

[24] Marder, M., (2006): *Supersonic rupture of rubber*, Journal of the Mechanics and Physics of Solids 54, 491–532.

[25] Nieves, M.J., Mishuris, G.S., Slepyan, L.I., (2016): *Analysis of dynamic damage propagation in discrete beam structures*, International Journal of Solids and Structures 97-98, 699-713.

[26] Nieves, M.J., Mishuris, G.S., Slepyan, L.I., (2017): *Transient wave in a transformable periodic flexural structure*, International Journal of Solids and Structures 112, 185–208.

Appendix

A Derivation of the governing equations in terms of generalised coordinates of the masses

The displacements W_m and $W_j^{\pm}$, along the horizontal and transverse beams, respectively, can be found by solving the equations

$$\frac{\mathrm{d}^4 W_m}{\mathrm{d}\tilde{x}^4}(\tilde{x}, t) = 0 , \quad 0 < \tilde{x} < a , m \in \mathbb{Z}$$

and

$$\frac{\mathrm{d}^4 W_j^{\pm}}{\mathrm{d}\tilde{y}_{\pm}^4}(\tilde{y}_{\pm}, t) = 0 , \quad 0 < \tilde{y}_{\pm} < a , j > Vt/a , j \in \mathbb{Z} ,$$

for $t > 0$, $\tilde{x} = x - am$, $\tilde{y}_+ = y$ and $\tilde{y}_- = y + a$. The function W_m satisfies the boundary conditions

$$W_m(0, t) = w_m(t) , \quad \frac{\mathrm{d}W_m}{\mathrm{d}\tilde{x}}(0, t) = -\theta_m^y(t) , \quad W_m(a, t) = w_{m+1}(t) \quad \frac{\mathrm{d}W_m}{\mathrm{d}\tilde{x}}(a, t) = -\theta_{m+1}^y(t) .$$

The function W_j^+ is subject to the conditions

$$W_m^+(0,t) = w_m(t) , \quad \frac{\mathrm{d}W_m^+}{\mathrm{d}\tilde{y}}(0,t) = \theta_m^x(t) , \quad W_m^+(a,t) = 0 , \quad \frac{\mathrm{d}W_m^+}{\mathrm{d}\tilde{y}}(a,t) = 0 ,$$

whereas W_j^- satisfies

$$W_m^-(0,t) = 0 , \quad \frac{\mathrm{d}W_m^-}{\mathrm{d}\tilde{y}}(0,t) = 0 , \quad W_m^-(a,t) = w_m(t) , \quad \frac{\mathrm{d}W_m^-}{\mathrm{d}\tilde{y}}(a,t) = \theta_m^x(t) .$$

Thus, from the above we have

$$\begin{aligned}
W_m(\tilde{x},t) &= -[a(\theta_m^y(t) + \theta_{m+1}^y(t)) - 2(w_m(t) - w_{m+1}(t))]\frac{\tilde{x}^3}{a^3} \\
&\quad + [a(2\theta_m^y + \theta_{m+1}^y) - 3(w_m(t) - w_m(t))]\frac{\tilde{x}^2}{a^2} - \theta_m(t)\tilde{x} + w_m(t) , \qquad \text{(A.1)}
\end{aligned}$$

and

$$W_m^+(\tilde{y}_+,t) = [a\theta_m^x(t) + 2w_m(t)]\frac{\tilde{y}_+^3}{a^3} - [2a\theta_m^x(t) + 3w_m(t)]\frac{\tilde{y}_+^2}{a^2} + \theta_m^x(t)\tilde{y}_+ + w_m(t) , \quad \text{(A.2)}$$

$$W_m^-(\tilde{y}_-,t) = [a\theta_m^y(t) - 2w_m(t)]\frac{\tilde{y}_-^3}{a^3} - [a\theta_m^x(t) - 3w_m(t)]\frac{\tilde{y}_-^2}{a^2} . \qquad \text{(A.3)}$$

The bending moments in the transverse beams applied about the x-axis can be calculated via

$$\mathcal{M}_m^{x,\pm}(\tilde{y}_\pm,t) = E_2 J_2 \frac{\mathrm{d}^2 W_m^\pm}{\mathrm{d}\tilde{y}_\pm^2}(\tilde{y}_\pm,t) .$$

The angular momentum balance about the y-axis for a mass in the supported region then gives

$$\mathcal{M}_m^{x,+}(0,t) - \mathcal{M}_m^{x,-}(a,t) = 0 ,$$

where the right-hand side is zero as it is assumed all masses have negligible moments of inertia. This together with (A.2) and (A.3) implies $\theta_m^x = 0$ in the supported region. The shear forces in these beams then have the form

$$\mathcal{V}_m^{y,\pm}(\tilde{y}_\pm,t) = -E_2 J_2 \frac{\mathrm{d}^3 W_m^\pm}{\mathrm{d}\tilde{y}_\pm^3}(\tilde{y}_\pm,t)$$

and using (A.2) and (A.3) leads to (6). The internal bending moments and shear forces in the m-th beam aligned with the horizontal axis, (see Figure 2) are computed via

$$\mathcal{M}_m^y(\tilde{x},t) = -E_1 J_1 \frac{\mathrm{d}^2 W_m}{\mathrm{d}\tilde{x}^2}(\tilde{x},t) \quad \text{and} \quad \mathcal{V}_m^y(\tilde{x},t) = -E_1 J_1 \frac{\mathrm{d}^3 W_m}{\mathrm{d}\tilde{x}^3}(\tilde{x},t), \qquad \text{(A.4)}$$

respectively. Insertion of (A.1) into these relations yields (4) and (5).

B An oscillating point force in an infinite mass-beam chain

Here, we derive the amplitude associated with the outgoing waves generated by point force in a mass-beam chain. The force is assumed to have frequency ω_0 and amplitude $\mathcal{P}_0$. According to the derivation of the governing equations in Section 2.2, the problem may be written as

$$\begin{aligned}
\frac{Ma^3}{E_1 I_1}\frac{\mathrm{d}^2 w_m(t)}{\mathrm{d}t^2} &= -6\left\{2[2w_m(t) - w_{m-1}(t) - w_{m+1}(t)] - a[\theta_{m+1}^y(t) - \theta_{m-1}^y(t)]\right\} \\
&\quad + \frac{a^3}{E_1 J_1}\mathcal{P}_0 \sin(\omega_0 t)\delta_{m,0} , \qquad \text{(B.1)}
\end{aligned}$$

and

$$3[w_{m+1}(t) - w_{m-1}(t)] + a[\theta^y_{m+1}(t) + \theta^y_{m-1}(t) + 4\theta^y_m(t)] = 0\,, \tag{B.2}$$

Here the Kronecker delta $\delta_{i,j}$ has been used to represent the position of the force in the structure. We consider the complex solution of this problem, i.e. we look for the solutions as

$$w_m(t) = \mathrm{Re}(\mathfrak{w}_m(t))\,, \quad \theta^y_m(t) = \mathrm{Re}(\vartheta^y_m(t)) \tag{B.3}$$

which allows use to consider the problem in terms of complex functions:

$$
\begin{aligned}
\frac{Ma^3}{E_1 I_1} \frac{\mathrm{d}^2 \mathfrak{w}_m(t)}{\mathrm{d}t^2} &= -6\left\{2[2\mathfrak{w}_m(t) - \mathfrak{w}_{m-1}(t) - \mathfrak{w}_{m+1}(t)] - a[\vartheta^y_{m+1}(t) - \vartheta^y_{m-1}(t)]\right\} \\
&\quad - \frac{a^3}{E_1 J_1} \mathrm{i}\mathcal{P}_0 e^{\mathrm{i}\omega_0 t}\delta_{m,0}\,,
\end{aligned}
\tag{B.4}
$$

and

$$3[\mathfrak{w}_{m+1}(t) - \mathfrak{w}_{m-1}(t)] + a[\vartheta^y_{m+1}(t) + \vartheta^y_{m-1}(t) + 4\vartheta^y_m(t)] = 0\,, \tag{B.5}$$

Here we non-dimensionalise the equations by introducing

$$\omega_0 = \sqrt{\frac{E_1 J_1}{Ma^3}}\omega\,, \quad \mathcal{P}_0 = \sqrt{\frac{E_1 J_1}{a^2}}P\,, \quad \mathfrak{w}_m = a\tilde{\mathfrak{w}}_m\,,$$

and assume the solutions take the form

$$\tilde{\mathfrak{w}}_m(t) = (-1)^m \mathcal{W}_m e^{\mathrm{i}\omega_0 t}, \quad \theta^y_m(t) = (-1)^m \Theta^y_m e^{\mathrm{i}\omega_0 t}\,. \tag{B.6}$$

We drop the "tilde" in going forward and derive the system

$$-\omega^2 \mathcal{W}_m(t) = -6\left\{2[2\mathcal{W}_m + \mathcal{W}_{m-1} + \mathcal{W}_{m+1}] + [\Theta^y_{m+1} - \Theta^y_{m-1}]\right\} - \mathrm{i}P\delta_{m,0}\,, \tag{B.7}$$

and

$$-3[\mathcal{W}_{m+1} - \mathcal{W}_{m-1}] + 4\Theta^y_m - \Theta^y_{m+1} - \Theta^y_{m-1} = 0\,. \tag{B.8}$$

In the following, the discrete Fourier transforms are used

$$\mathcal{W}^F = \sum_{m=-\infty}^{\infty} \mathcal{W}_m e^{\mathrm{i}km} \quad \text{and} \quad \Theta^{y,F} = \sum_{m=-\infty}^{\infty} \Theta^y_m e^{\mathrm{i}km}\,.$$

We take the discrete Fourier transform to obtain

$$[-24(1 + \cos(k)) + \omega^2]\mathcal{W}^F + 12\mathrm{i}\sin(k)\Theta^{y,F} - \mathrm{i}P = 0\,, \tag{B.9}$$

and

$$6\mathrm{i}\sin(k)\mathcal{W}^F + 2(2 - \cos(k))\Theta^{y,F} = 0\,. \tag{B.10}$$

Combining (B.9) and (B.10) we obtain

$$\mathcal{W}^F = -\frac{\mathrm{i}P}{h_2(k, \mathrm{i}\omega)}$$

and following the inverse discrete Fourier transform, we have

$$\mathcal{W}_m = -\frac{\mathrm{i}}{2\pi} \int_{-\pi}^{\pi} \frac{P e^{-\mathrm{i}km}}{h_2(k, \mathrm{i}\omega)}dk\,.$$

For outgoing waves from the source to exist we require that $\omega < \sqrt{48}$. In this case, in the interval $-\pi < k < \pi$ the chosen load frequency can be linked to with two wave numbers $\pm k_f \mp \mathrm{i}0$, that defined the waves propagating in the medium. These wavenumbers are singular points of the kernel in the above integral. The above is then rewritten as

$$\mathcal{W}_m = -\frac{\mathrm{i}}{2\pi} \int_{-\pi}^{\pi} \frac{P e^{-\mathrm{i}km}}{(0 - \mathrm{i}(k - k_f))(0 + \mathrm{i}(k + k_f))R_0(k,\omega)} dk \ ,$$

where the function R_0 is defined in (32) and has no real zeros or poles on the real axis. Applying the residue theorem, under the assumption $m \to \infty$, the integral on the right-hand side has the asymptote

$$\frac{1}{2\pi} \int_{-\pi}^{\pi} \frac{P e^{-\mathrm{i}km}}{(0 - \mathrm{i}(k - k_f))(0 + \mathrm{i}(k + k_f))R_0(k,\omega)} dk \sim \frac{\mathrm{i}P e^{-\mathrm{i}k_f m}}{2k_f R_0(k_f,\omega)} \ , \qquad \text{for } m \to \infty \ .$$

Combining this with (B.6) and (B.3) we have

$$w_m(t) \sim \frac{P}{2k_f R_0(k_f,\omega)} \cos((k_f + \pi)m - \omega_0 t) \qquad \text{for} \quad m \to \infty \ .$$

Thus, from this we see that the amplitude of the feeding wave in the problem considered in Section 5 is

$$A = \frac{P}{2k_f R_0(k_f,\omega)} \ ,$$

where the variables in this expression are dimensionless.